# Ανάπτυξη Μικροακίδων Πυριτίου με Laser

## Βασιλεία Ζορμπά

## Μεταπτυχιακή Εργασία

Πανεπιστήμιο Κρήτης
Σχολή Θετικών Επιστημών
Τμήμα Φυσικής



Μεταπτυχιακό Πρόγραμμα
Μικροηλεκτρονικής-Οπτοηλεκτρονικής

ΗΡΑΚΛΕΙΟ 2003

Πανεπιστήμιο Κρήτης
Σχολή Θετικών Επιστημών
Τμήμα Φυσικής

Μεταπτυχιακό Πρόγραμμα
Μικροηλεκτρονικής-Οπτοηλεκτρονικής

# Ανάπτυξη Μικροακίδων Πυριτίου με Laser

## Μεταπτυχιακή Εργασία
Βασιλεία Ζορμπά

Επιβλέπουσα Ερευνήτρια: Ι. Ζεργιώτη
Υπεύθυνος Καθηγητής : Κ. Φωτάκης

ΗΡΑΚΛΕΙΟ 2003

University of Crete
School of Sciences
Department of Physics

Postgraduate Course
in Microelectronics and Optoelectronics

# Laser induced Si Micro-spikes Fabrication

## Master Thesis
Vasilia Zorba

Thesis Advisor: I. Zergioti
Thesis Supervisor : K. Fotakis

HERAKLION 2003

# ΕΥΧΑΡΙΣΤΙΕΣ

Η εργασία αυτή είναι το αποτέλεσμα της συνεργασίας μιας ομάδας ανθρώπων, στους οποίους και θα ήθελα να εκφράσω τις ευχαριστίες μου. Θα ήθελα αρχικά να ευχαριστήσω τον Καθ. Κ.Φωτάκη, διευθυντή του Ι.Η.Δ.Λ. του Ι.Τ.Ε., ο οποίος μου έδωσε την ευκαιρία να εργαστώ στα εργαστήρια λέιζερ, με προέτρεψε να ασχοληθώ με τον τομέα της κατεργασίας υλικών με λέιζερ, και είχε και την γενικότερη εποπτεία της εργασίας αυτής.

Ένα μεγάλο ευχαριστώ θα ήθελα να εκφράσω στην Δρ. Ιωάννα Ζεργιώτη, πρώην Ερευνήτρια Δ' του Ι.Η.Δ.Λ. και νυν Λέκτορα του Τμήματος Εφαρμοσμένων Μαθηματικών κι Φυσικών Επιστημών του Εθνικού Μετσόβιου Πολυτεχνείου, η οποία υπήρξε και η άμεση επιβλέπουσα της εργασίας αυτής. Η επιστημονική της καθοδήγηση υπήρξε για μένα πραγματικά ουσιαστική. Ιδιαιτέρως την ευχαριστώ για την ενθαρρυντική της στάση και για την εμπιστοσύνη που έδειξε σε εμένα.

Ένα ευχαριστώ οφείλω στην Αλέκα Μανουσάκη για τη σημαντική (και ιδιαίτερα ευχάριστη) συνεισφορά της στον μορφολογικό χαρακτηρισμό των δειγμάτων. Επίσης θα ήθελα να ευχαριστήσω τον Δρ. Ιωάννη Αλεξάνδρου του Engineering Department του πανεπιστημίου του Cambridge για την πολύτιμη συμβολή του στις ηλεκτρικές μετρήσεις των δειγμάτων. Ένα μεγάλο ευχαριστώ θα ήθελα να εκφράσω στον Μανώλη Σκαντζάκη, προπτυχιακό φοιτητή του Τμήματος Εφαρμοσμένων Μαθηματικών κι Φυσικών Επιστημών του Εθνικού Μετσόβιου Πολυτεχνείου, για την συνεργασία που είχαμε στην τέλεση των πειραμάτων. Μέρος της δουλειάς αυτής αποτέλεσε και το αντικείμενο της πρακτικής του άσκησης.

Δε θα πρέπει να παραλείψω να εκφράσω τις ευχαριστίες μου σε όλους τους μεταπτυχιακούς φοιτητές του εργαστηρίου των λέιζερ. Το φιλικό κλίμα το οποίο επικρατεί, κάνει την εργασία στο συγκεκριμένο χώρο πολύ πιο ευχάριστη και εποικοδομητική. Τέλος ένα μεγάλο ευχαριστώ θα ήθελα να εκφράσω, στους Νίκο Βουλγαράκη, Κέλλυ Γιαννακουδάκη, Όλγα Κοκκινάκη, Μαρία Σπυριδάκη και Γιώργο Χατζησάββα, η υποστήριξη και η βοήθεια των οποίων, με τον ένα τρόπο ή με τον άλλο, ήταν για μένα πολύτιμη.

Βασιλεία Ζορμπά
Νοέμβριος 2003

# TABLE OF CONTENTS:

# SUMMARY

Cumulative laser irradiation of silicon wafers in a reactive gas atmosphere is known to give rise to the formation of dense arrays of high aspect ratio silicon (Si) micro-pyramids (spikes). This work examines the possibility of controlling the tip radius and aspect ratio of the obtained structures achieved by optimizing the laser and ambient gas pressure ($SF_6$) conditions. In particular, Si spikes were grown by using lasers of different wavelength and pulse duration. A comparative study between ns (XeCl, 308nm) and fs (Ti:Sap., 800nm; KrF, 248nm) laser sources is presented.

The obtained conical Si features exhibited a rather homogenous distribution and a spontaneous self-alignment into arrays. Their tip diameter was down to 500nm while their height reached up to 30 μm. When tested as cold cathode field emitters these structures showed a field emission threshold as low as 2 V/μm, with an emission current of $10^{-3}$ A/cm$^2$ at 4 V/μm. Even though these structures have smaller aspect ratios than good quality carbon nanotubes, their field emission properties are similar. The simple and direct formation of field emission Si arrays over small preselected areas by laser irradiation could lead to a novel approach for the development of electron sources.

# CHAPTER 1

## INTRODUCTION AND OVERVIEW

## 1.1 INTRODUCTION

Silicon (Si) based devices constitute the basis for the rapid development of the microelectronics technology during the past decades. Si-based technology, at this point, has reached a level of maturity, and finds several applications in industrial scale. To this effect, the processing of Si surfaces for inducing morphological and structural modifications, such as to alter its surface properties, is of particular interest. These alterations open up the possibility of expanding the use of inexpensive Si in a variety of novel devices.

It has been shown that structuring of Si surfaces, in such a way as to form arrays of microtips, may alter its properties in a beneficial manner. More specifically, microstructured Si, otherwise known as "black silicon", exhibits altered optical properties (increased absorption throughout a wide range of wavelengths) as compared to the untreated Si surfaces. However, differences in the electrical properties have been observed as well. Based on such differences it has been shown that microstructured Si may be a good candidate as an efficient field emitter source.

Silicon based electron emitters have recently attracted interest because of their easy integration to the existing Si-based vacuum microelectronic processes, that may allow the deep miniaturization. Furthermore, Si based field emitters do not require ultrahigh vacuum for long lifetime operation. Periodic arrays of microtips of this sort are commonly used as cold cathode field emitters in integrated circuits, flat-panel displays and microwave power amplifiers. Traditionally, they are structured by means of lithography.

A novel approach to cold cathode field emitter manufacturing, is the utilization of laser pulses for the formation of these Si microstructures (or so-called Si spikes), in a reactive gas atmosphere (such as $SF_6$). This allows areas from tens of

microns to tens of millimeters in diameter to be microstructured without the use of lithographic masks. Furthermore, no ultrahigh vacuum or cleanliness conditions are required throughout the fabrication process. This technology prompts fairly reproducible average spacing, height and aspect ratio of the conical microstructures obtained.

This work investigates the interaction of laser pulses with different pulse durations, within the range of nanosecond (ns) to femtosecond (fs), with Si surfaces in the presence of a reactive gas ($SF_6$). More specifically, three laser sources have been employed for the purposes of this work; a ns XeCl ($\lambda=308nm$, $\tau_{FWHM}=32ns$) eximer laser source, a sub-ps KrF ($\lambda=248nm$, $\tau_{FWHM}=500fs$) excimer laser source and a regenerative amplified fs Ti:Sapphire *($\lambda=800nm$, $\tau_{FWHM}=50fs$)* laser source. The optimization of the Si spikes field emission properties was an objective. Therefore, emphasis has been given on the optimization of silicon spikes formation conditions (laser and ambient gas pressure parameters) on the basis of homogeneity and aspect ratio maximization, in a controlled and reproducible manner. This work puts into evidence the possibility of utilizing these laser produced structures as basic components of directional electron beam sources.

## 1.2 CONTENT AND ORGANIZATION

This thesis is structured as follows:

*Chapter 2* focuses on field emission from conical microstructures. A short review of the fundamental theory describing field emission from metals and semiconductors is given, while the shape and characteristics of an ideal field emitter are discussed. Moreover, the properties of Si based microtip field emitters as well as the numerous advantages they exhibit are examined, in combination with some of the extensively implemented techniques for their fabrication. A comparison with laser based methods for Si spikes fabrication is given on this basis, while the potential of employing these structures as basic components in applications such as field emission displays and microwave amplifiers, is acknowledged.

*Chapter 3* examines the stages of laser induced conical microstructures evolution in reactive gas atmospheres. The basic laser-solid interactions from a macroscopic and microscopic point of view are reviewed. Moreover, the Laser Induced Periodic Surface Structures (LIPSS) are introduced and their contribution, along with that of the reactive gas, to the formation of Si spikes, is given. Previous studies and advances on the field of Si microstructuring, are also reviewed.

*Chapter 4* presents a short description of the experimental apparatus implemented for the purposes of this work. Furthermore it presents the characterization techniques and instrumentation for obtaining information concerning the morphology and field emission of the Si microstructures obtained.

*Chapter 5* includes the experimental results obtained in the course of this work. The different stages of spikes evolution are studied in detail. Moreover, the influence of laser and ambient gas ($SF_6$) parameters on the quality of the obtained structures, as well as their contribution in defining their properties in a controlled and reproducible manner, was considered. Results concerning structures obtained utilizing three laser sources with different pulse durations (ns, sub-ps, fs) are discussed, while possible mechanisms operative during microstructuring of Si surfaces are given. Moreover, these structures are tested as cold cathode field emitters, and in this context field emission data are presented.

Finally, *Chapter 6* includes the concluding remarks as well as prospects of future experiments on the field

# CHAPTER 2

## FIELD EMISSION FROM CONICAL MICROSTRUCTURES

## 2.1 INTRODUCTION

Vacuum microelectronics is a relatively new interdisciplinary field utilizing the mechanism of electron emission into a vacuum for devices requiring bulk and surface micromashining. By fabricating arrays of conductive or semiconductive structures that are either gated or ungated, a multitude of devices can be formed that utilize cold emission and ballistic transport of electrons from emitting cathodes to appropriate collector electrodes. Potential applications include flat panel vacuum fluorescent displays, ultrahigh-frequency power sources and amplifiers, high-speed logic and signal processing circuits, and sensors. The technology of vacuum microelectronics may be capable of operation within extremely harsh environments in terms of temperature and radiation [1].

A wide range of materials placed at different geometries have been considered as cold cathode field emitters. Metal-insulator-vacuum (MIV) structures, thin flms, diamond and diamond films, graphite and graphite pastes, polymers, carbon fibres and nanotubes are just several of the materials tested so far. However, the most familiar structure of a cold cathode field emitter is an array of microtips or Spindt tips named after Capp Spindt who first described the fabrication of these structures back in 1968 [2].

In this chapter the use of conical silicon microstructures as potential field emitters is discussed. The fundamental theory of field emission from metals and semiconductors as well as the shape and characteristics of an ideal field emitter are briefly reviewed. The properties of Si based microtip field are examined, while techniques implemented for their fabrication are discussed. Finally, in the end of this chapter some of the most interesting potential applications are exhibited.

## 2.2.THEORY OF FIELD EMISSION

Field emission refers to the emission of electrons from a solid cathode (generally in the shape of a sharp tip) into vacuum under the influence of a strong electric field [3]. The pointed or conical shape of the cathode strongly enhances the electric field at the tip, which is the result of biasing the cathode with respect to a nearby anode. Field emission occurs when electrons tunnel through the potential energy barrier at the interface between the cathode and the vacuum. This is in contrast with the more familiar phenomenon of thermionic emission, wherein electrons are emitted from a cathode when they have sufficient thermal energy to pass over the potential barrier.

### 2.2.1 Field-emission from a metal

We first consider the case of field emission from a metal. The relevant energy level diagrams are shown in Fig. 2.1, where the potential energy as a function of position for an electron near a metallic surface is shown for three different electric field regimes [4]. Within the metal, energy states up to the Fermi energy $E_F$ are occupied. In the vacuum, the lowest accessible level is at an energy $E_F + \Phi$, where $\Phi$ is the work function of the metal.

Figure 2.1 shows the energy barrier between a metal and vacuum. Thermionic emission is shown by A. The field there is very small, so no deformation of the energy barrier $\Phi$ takes place. Only electrons that acquire enough thermal energy from heating the emitter can overcome the barrier. At higher fields and still elevated temperatures, the barrier is deformed (the potential energy in the vacuum is now a linear function of distance from the metal-vacuum interface) and field dependant emission caused by barrier lowering due to the image charge takes place. This is shown in B and is known as Schottky emission [5]. As the field increases, the barrier continues to become lower, but also narrower. Under specific conditions (concerning the material work function and the applied field), the

barrier may become sufficiently narrow that electrons can tunnel through it, even at T=0 K. This is known as field emission and is shown by C.
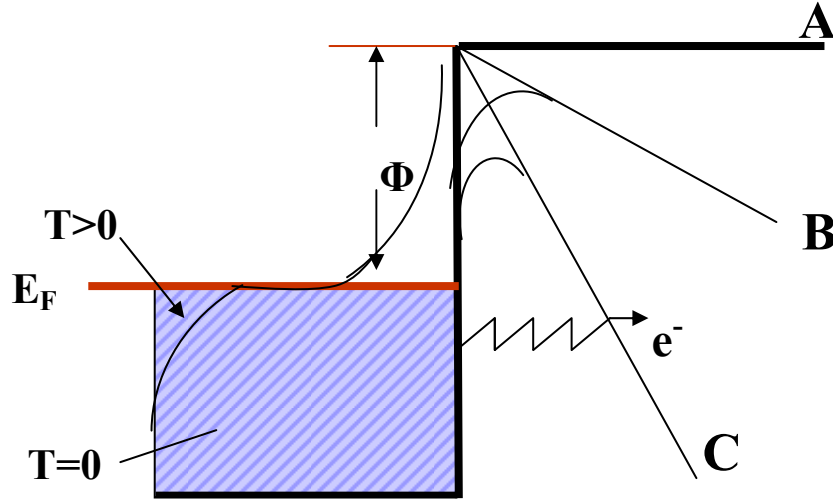


Fig. 2.1- Energy diagram for thermionic emission (A), Schottky emission (B) and field emission (C). The electron distributions in the emitter are plotted for the cases T=0 K and elevated temperature T> 0 K. $E_F$ is the Fermi energy of the metal and Φ is the barrier height or work function

A qualitative understanding of the tunnelling phenomenon can be gained from the Heisenberg uncertainty principle.  Supposing that the electrons can escape from the solid to the field-free vacuum along the x-direction and $E_F$ is the energy at the Fermi level, the potential barrier a valance electron has to overcome in order to leave the material is:

$$E_B = E_F + \Phi - E_x \qquad (Eq.\ 2.1)$$

where $E_x$ is the kinetic energy of the electron along the x-direction. In thermionic emission and photoemission [10], where the surface potential has not been modified, the barrier is so high that tunnelling of electrons through it is impossible. Therefore an electron needs to be given an energy equal to $E_B$ in order to be emitted from the material. However in the presence of a very strong external electric field, $\varepsilon$ , the width, ω, of the potential barrier is modified according to the equation:

$$\omega = \frac{E_F + \phi - E_x}{\mathcal{E} \cdot e} \qquad \textit{(Eq. 2.2)}$$

where e is the charge associated with a single electron. Small values of ω and $E_B$ make it possible for the electrons to pass "through" the barrier (tunneling) rather than having to climb over it.  An electron within the metal, with a kinetic energy of $E_x$ due to its velocity in the *x*-direction, experiences a potential barrier at the metal-vacuum interface with height $E_F + \Phi - E_x$ and width $(E_F + \varphi - E_x) / \mathcal{E}$ e.

According to Heinsenberg's principle there is an uncertainty in defining the momentum, Δp, and position, Δx, of an electron, which is described by the famous equation:

$$\Delta x \cdot \Delta p = \frac{\eta}{2}, \quad \text{with} \quad \eta = \frac{h}{2\pi} \qquad \textit{(Eq. 2.3)}$$

If we consider an electron with an energy near the Fermi level, the uncertainty in momentum stems from defining its energy, $E = \Delta^2 p / 2m$, within the energy gap Φ. For this energy uncertainty to result in a kinetic energy that equals the barrier height, the corresponding momentum uncertainty is $\Delta p = \sqrt{2 \cdot m \cdot \phi}$, where E has been substituted by $E_F$, and m is the rest mass of the electron. According to equation 2.3, the corresponding uncertainty in position is:

$$\Delta x = \frac{\eta}{2 \cdot \Delta p} = \frac{\eta}{2 \cdot \sqrt{2 \cdot m \cdot \phi}} \qquad \textit{(Eq. 2.4)}$$

If Δx is greater or equal to ω, then there is a finite possibility that the electron will be found on either side of the surface of the material. Combining Eqs. 2.2 and 2.4 the condition for field emission is roughly:

$$\frac{\eta}{2\sqrt{2 \cdot m \cdot \phi}} \geq \frac{\phi}{\mathcal{E} \cdot e} \qquad \text{or}$$

$$\boxed{\mathcal{E} \geq \sqrt{\frac{8m}{\eta^2 \cdot e^2}} \phi^{3/2}} \qquad \textit{(Eq. 2.5)}$$

for an electron at the Fermi level.

However, a more detailed analysis of the probability for electron tunneling requires the application of more complex quantum mechanics. Implementing the Schrodinger equation in this one-dimensional motion of the electron, we have:

$$\frac{d^2\psi}{dx^2} + \frac{2 \cdot m}{\eta^2} E \cdot \psi = 0 \qquad\qquad (Eq.\ 2.6)$$

inside the metal and

$$\frac{d^2\psi}{dx^2} + \frac{2 \cdot m}{\eta^2}\left[\ E - (\Phi + E_F) + \mathcal{E}\ \right] \cdot \psi = 0 \qquad\qquad (Eq.\ 2.7)$$

outside the metal and within the potential barrier, where E is the kinetic energy in the x-direction and $\psi$ is the wave function of the electron. $\Phi$ is the work function of the material, $E_F$ is the energy difference between the highest state of the valance band and the Fermi level and $\mathcal{E}$ is the externally applied electric field. These two equations are solved by applying the boundary conditions that $\psi$ and $d\psi/dx$ are continuous at x=0. The solution inside the potential barrier is an attenuating wave and is given here as a function of the electron energy E:

$$D(E_x) = \frac{4\left[Ex \cdot (E_F + \Phi - E_\chi)\right]^{1/2}}{E_F + \Phi} \cdot \exp\left[ -\frac{4}{3} \cdot \left(\frac{2m}{\eta^2}\right)^{1/2} \cdot \frac{(E_F + \Phi - E_x)^{3/2}}{\mathcal{E} \cdot e} \right]$$

$$(Eq.\ 2.8)$$

The emitted current density is found by multiplying this tunnelling probability by the rate of arrival at the barrier of electrons with energy $E_x$ (Fermi-Dirac distribution), and then integrating over the energy range $0 \le E_x \le E_F$ . The resulting equation, first described in 1928, is the so-called Fowler-Nordheim expression (Eq. 2.9).

$$J = A \cdot \mathcal{E}^2 \cdot \exp\left[\frac{B}{\mathcal{E}}\right] \qquad\qquad (Eq.\ 2.9)$$

with $A = 6{,}2 \times 10^{-2}\ \dfrac{\left[\ \dfrac{E_F}{\Phi}\ \right]^{1/2}}{E_F + \Phi}$

$B = -6{,}8 \times 10^{11} \times\ \Phi^{3/2}$

When the applied field $\varepsilon$ is amplified, then quantity B becomes $-6{,}8 \times 10^{11} \times \dfrac{\Phi^{3/2}}{\beta}$

Here, $\beta$ $(\beta>1)$ is a geometrical factor describing the field enhancement at the sharp tip. All energies are measured in eV, current density J in Amp/cm$^2$ and the electric field $\varepsilon$ in V/µm.

The Fowler-Nordheim equation is a useful tool for evaluating the origin of a given emission current (i.e. field emission, thermionic emission or even photo-emission). If the current emitted from the cathode is attributed to field emission, it is expected to follow the $\varepsilon$ -dependence described in Equation 2.9. Thus, we can plot $ln(J/\varepsilon^2)$ *vs.* $1/\varepsilon$ and expect a linear relation if the current $J$ is the result of field emission. The values $A$ and $B$ can also be extracted from the slope and *y*-intercept of the linear Fowler-Nordheim plot.


## 2.2.2 Field-emission from a semiconductor

Field-emission from a semiconductor is described by a very similar theory to that for the field emission from a metal, as summarized above in the Fowler-Nordheim equation. However, the more complicated energy bandstructure in a semiconductor leads to a few important modifications. Figure 2.2 illustrates the energy states of the semiconductor near the semiconductor-vacuum interface.
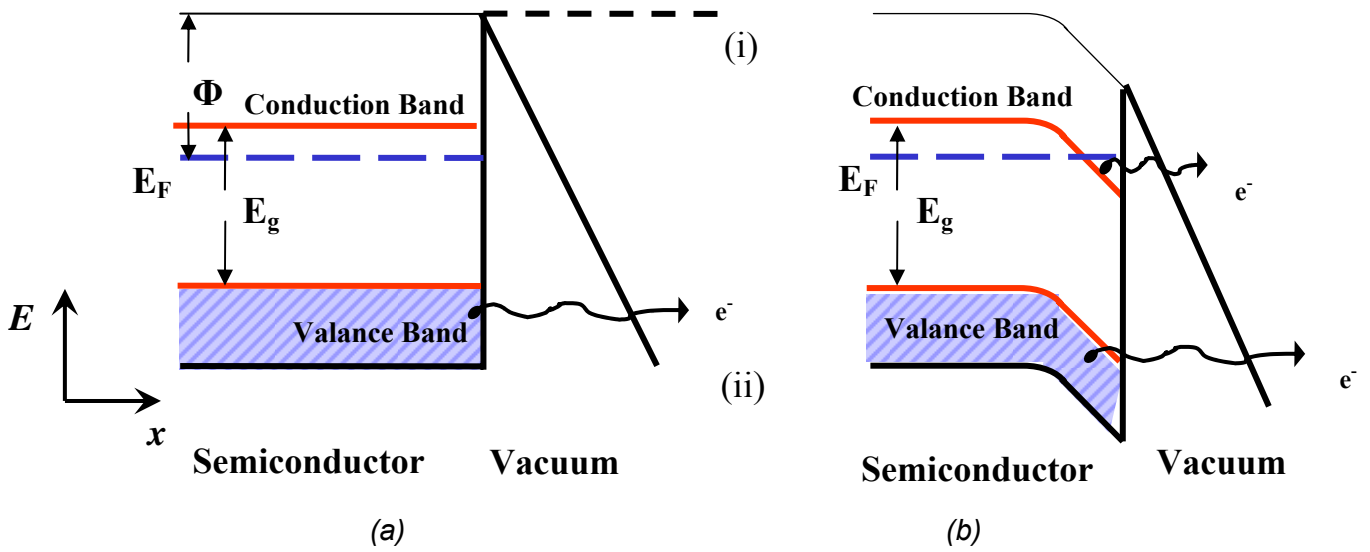
Fig. 2.2- Potential energy of an electron vs. position near a semiconductor surface. Energy states of semiconductor near the semiconductor-vacuum interface: (a)(i) without an applied field, (ii) in the presence of an applied field and  (b) in the presence of an applied field with its penetration into the surface taken into account

When the penetration of the applied electric field is neglected, tunneling can occur from the valence band if the applied field is sufficiently intense as illustrated in Fig. 2.2 (a)-ii. In this case, the current obeys Fowler-Nordheim behavior, having however an effective work function $\Phi_{effective} = \Phi + E_g$, $E_g$ being the bandgap of the semiconductor. In the case when the conduction band is thermally occupied, tunneling also takes place from the conduction band, but this is not usually the case.

Still, if the penetration of the applied electric field into the semiconductor is taken into account, the picture becomes somewhat more complicated. The electric field in this case can cause the deformation of the potential experienced by the electrons (Fig. 2.2 (b)). If the deformation is strong enough, the bottom of the conduction band comes to be at a lower energy than the Fermi energy on the semiconductor side of the interface, and electrons accumulate in the dip in the conduction band. Tunneling must then be consider, and sequentially field emission, from two distinct groups of electrons, those in the valence band and those in the dip in the conduction band. Field emission attributed to the conduction band electrons follows Fowler-Nordheim behavior with an effective work function

$\Phi_{effective} = \Phi - (E_F - V_0)$, $V_0$ being the energy by which the bottom of the conduction band is shifted in the presence of the applied field. Clearly, the electrons in the altered conduction band can be induced to tunnel through the barrier by a lower electric field than must be used to induce tunneling by the valence-band electrons. Thus, in some cases, two regimes of field-emission are considered for two regimes of applied field strength.

### 2.2.3 Field Emission Properties Optimization

According to the Fowler-Nordheim equation, there is an exponential relation correlating the emitted electron current density (J) to a factor beta (β) describing the field enhancement at the sharp tip. Consequently, the field enhancement due to geometrical factors is expected to decrease the magnitude of the external electric field required to commence field emission (i.e. the threshold field $\epsilon_{th}$). This observation has drawn interest in to machining field emitters into protruding objects so as to take advantage of field enhancement of regions of high curvate. Accordingly, in order reach  high fields at reasonable voltages one should  move primarily towards the direction of aspect ratio maximization (i.e. height/tip radius).

However, of interest is the thinking that the beta factor is not simply a geometrical enhancement factor governed entirely by surface morphology, but it can be dictated by internal structure such as micro-inclusions, changes in the chemical bonding and grain boundary structures [6]. The Fowler-Nordheim equation has been repeatedly referred to in papers studying field electron emission from semiconductors and composite solids. Still the simple form often quoted is not always applicable when an exact and a detailed analysis is required [7]. Nevertheless, the employment of this expression is a very useful tool for an estimative analysis. A recent and detailed study of the applicability of the Fowler-Nordheim equation to field electron emission from a variety of materials has been published by Forbes [8].

### *2.2.4 The ideal field emitter structure*

The performance of a field emitter, however, is not merely dependant on the aspect ratio of the microstructures that it consists of. It is also strongly dependant on the shape of the potential emitter.

Different emitter shapes have been analyzed by Utsumi [9], who introduced a so-called "merit factor" to compare their performance. As shown in Fig. 2.3 (b), the highest f=1 value is attributed to the ideal emitter represented by the floating sphere model (FSM), Fig. 2.3 (a). The highest next value f=0,6 corresponds to a rounded post emitter like a whisker. The technologically feasible emitter closest in shape to the whisker is the "Eiffel tower" shaped, Fig. 2.3 (b). Sequentially interest has been drawn towards fabricating emitters of this kind: tall, narrow and with small tip curvate radius.
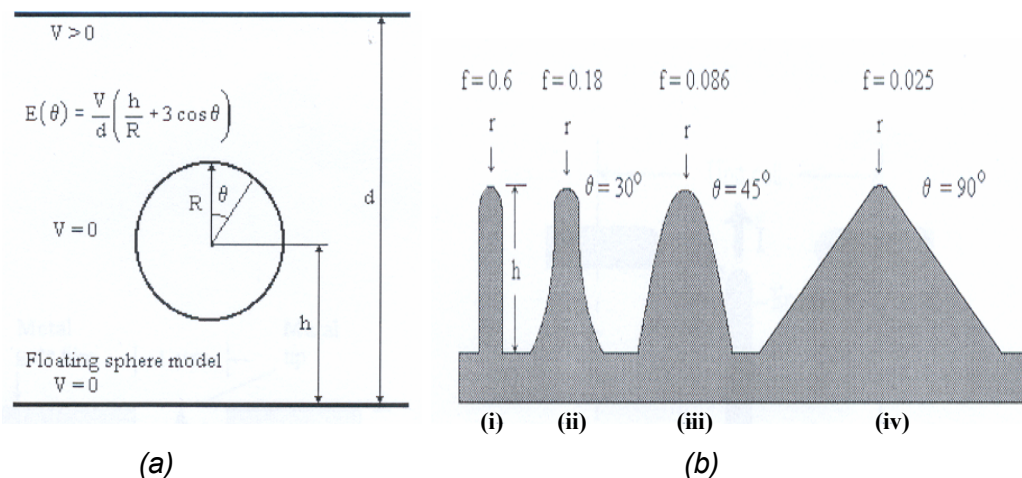


Fig 2.3 – (a) The floating sphere field emitter model and (b) Various shapes of field emitters and their figures of merit: (i) rounded whisker; (ii) sharpened pyramid; (iii) hemispheroidal protrusion; (iv) pyramidal field emitter

## 2.3 Si Based Microtip Field Emitters

Until recently, metals have mostly been considered as potential cold cathode electron sources. However the possibility of utilizing semiconducting materials has been acknowledged. In particular Si has attracted great interest, owing to its

unique properties; that is silicon is a relatively cheap, well characterized material. In addition Si is a material which can be easily doped, allowing in this manner its properties to be accordingly altered. Furthermore, fabrication of Si field emission arrays can take advantage of the existing wealth of knowledge of Si processing techniques and also allow their easy integration to Si existing technology. Contrary to metal based field emitters, Si based emitters can operate under conditions of low vacuum and cleanliness.

## 2.4 SPINDT TIP ARRAYS FABRICATION

The interest in utilizing microtip arrays as cold cathode field emitters has been displayed. Nevertheless the fabrication technology used for obtaining a given structure always has to be accounted for. When evaluating the potential of a new fabrication technology, several factors should be considered, such as how precise and reproducible it is, and also its suitability for (large) emitter arrays manufacturing and integrating with complementary circuits [10].

Traditionally, microtip arrays for large area electron sources are fabricated using the Spindt tip process, based on lithography. This technology prompts well defined, high quality structures. In this context, this process of microtip array fabrication has proven to be quite effective. However it is a multi-step process involving clean room facility requirements.

A novel approach to cold cathode field emitters manufacturing is the use laser irradiation of Si surfaces in the presence of a reactive gas, for the formation these periodic surface structures. This is a simple one-step production method of quasi-periodical micro-tip arrays yielding reproducible average spacing, height and aspect ratio of the obtained microstructures, under conditions of reduced atmosphere, without sophisticated vacuum equipment requirements. The process and dynamics of Si spikes formation is discussed in the following chapter.

## 2.5 APPLICATIONS OF MICROTIP EMITTER ARRAY BASED DEVICES

Devices based on field emission feature many desirable characteristics. Field emitters can produce electron beams with high brightness and current density while operating at low voltages and consecutively consuming relatively little power. They can be integrated into small, lightweight devices and can be operated at high repetition rates due to their rapid on/off switching speed.

A number of applications take advantage of the field emission current from a single sharp tip or array of tips. A few of the most interesting applications of single tips and arrays are reviewed, including field emission displays and microwave sources.

### 2.5.1 Field emission displays

Field emission displays are thin, flat cathode ray tubes consisting of two-dimensional matrix electron sources (the pixels), which illuminate a monochromic or full-colour screen. Each pixel has about a thousand tips (a density of $10000/mm^2$). The first FED to work at television data rates was demonstrated by in 1991, while full colour version appeared two years later.

The device uses molybdenum Spindt-type microtip arrays deposited on a glass substrate. Below the tips, a resistive sheet and a structured metallic mesh, maintain a homogeneous electron emission and protect the tips, either by limiting the emitted current or by functioning as local micro-fuses. In the case of full colour, low voltage FEDs, three anodes are successively switched; and in this way colour purity is obtained without the need to refocus the individual electron beams. One other advantage of this structure is the reduction in the number of drivers by a factor of three (one single emitter sends electrons towards a sub-pixel which is successively red, green and blue).
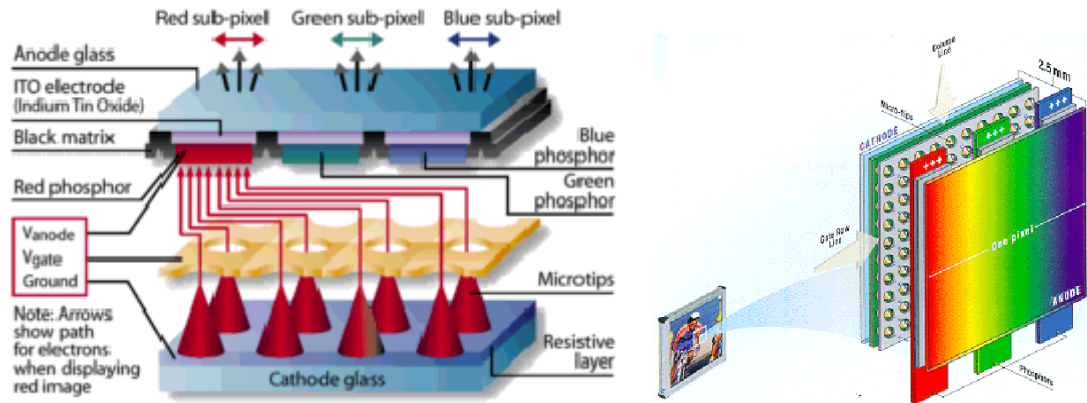
Fig. 2.4- The Field Emission Display principle of operation.

The advantage of this technology, apart from needing less power, is that the displays are thin and light. Although it has the optical quality of a cathode ray tube, it does not produce X-rays, nor is it sensitive to magnetic fields or large temperature variations. For all of these reasons it can find wide range of applications in industrial and automobile applications or as monitor for scientific and medical instruments (such as mass spectrometers or oscilloscopes). Versions have also been developed for avionics and this technology could possibly be considered for manned space systems.

### 2.5.2 Microwave applications

The performance of a radio frequency power amplifier tube can be significantly enhanced if it contains a cathode capable of producing current densities much greater than 10 A/cm$^2$, emission modulated at microwave frequencies. High density, small aperture, field emitter array (FEA) are capable of this.

Field emitter arrays may offer higher transconductance and higher current densities than those achieved with thermionic cathodes, and can greatly improve the performance of girded microwave power amplifier tubes. Furthermore these devices minimise the need for high voltage power supplies and heavy magnets, commonly found in linear tubes. Travelling wave tubes employing field emitter array cathodes are now being designed to provide 100 W output power at 10 GHz with 10 dB power gain and an efficiency exceeding 50%.

Wide band, high-efficiency and compact radio frequency sources have many applications in space, mobile communications and high speed data networking. In a microwave transmitter, the electron tube is a key component, which mainly influences the radio frequency performance, efficiency and lifetime of the equipment. A field emitter array travelling wave tube can make an important contribution to a communications satellite

# CHAPTER 3

# LASER INDUCED SI CONICAL MICROSTRUCTURES

## 3.1 INTRODUCTION

Laser-induced "damage" of solids has been of scientific and technological interest since the development of the laser [11]. Absorption of laser irradiation by a solid can lead to a permanent modification of its surface, causing melting and resolidification, vaporization, or ablation of the material. Laser induced "damage" has been studied over the years for a wide range of materials including metals [12,13], semiconductors [32, 14] and dielectrics [15]. The exploitation of laser light's unique properties has pointed out its utility in altering the materials properties in a beneficial manner. Accordingly the possibility of materials processing using both continuous and pulsed lasers has long been recognized.

Today abrasive laser machining (e.g. drilling, scribing, cutting, trimming and shaping), laser induced morphological, structural and compositional transformations of material surfaces (e.g. annealing, glazing) and processing applications that involve an overall change in the chemical composition of the surface (e.g. cladding), are examples indicating how laser-material interactions may be exploited for materials properties modification.

This chapter examines the formation of elongated quasi-periodical Si microstructures utilising laser pulses in a reactive gas atmosphere. A review of the basic laser-solid interactions is presented and an interpretation of the resulting phenomena is considered from a microscopic and macroscopic point of view. Laser induced periodic surface structuring is introduced and its role in the formation of Si microstructures is reviewed. Moreover the synergy of laser assisted chemical etching (due to the existence of the reactive gas) to Si spikes development is acknowledged. Finally an overview on the previous studies on Si

microtip array fabrication and advances in this field, is given in the end of this chapter.

## 3.2 LASER-SOLID INTERACTIONS: FUNDAMENTAL ASPECTS

The interpretation of the basic interaction mechanisms between the intense light of a laser beam and matter, is an aspect of most interest [2]. Laser light and matter interaction mechanisms are strongly dependant on the laser beam parameters (i.e. wavelength, pulse duration, intensity, spatial and temporal coherence, polarization etc.), the physical and chemical properties of the material employed (absorption coefficient, thermal diffusion, heat of vaporization etc.), as well as on the environmental conditions (vacuum, reactive or non-reactive surrounding medium). These parameters determine the type of elementary excitations and the interaction between them.

### 3.2.1 Primary Processes

The first step in any structural modification of a material by laser irradiation is the deposition of a certain amount of laser energy. The total laser energy and the spatial and temporal energy distribution determine what kind of final modification will be obtained [16].

The initial interaction of laser pulses with a solid is the excitation of electrons. Upon photon absorption electrons are excited from their equilibrium states into higher-lying unoccupied states. Optical excitation in a semiconductor solid is described by four basic processes as illustrated in Fig. 3.1.

The electrons can undergo interband transitions by (*a*) single-photon excitation, (*b*) multi-photon excitation or (*c*) intraband transitions by free-carrier excitation. Free-carrier excitation refers to the linear absorption of several photons by a conduction band electron, sequentially moving to higher states in the conduction band. Single-photon band-to band excitation is the primary process whereas the latter two become increasingly significant with increasing laser intensities. It is clear that for a given laser fluence a shorter pulse duration favors multiphoton

excitation processes, as the probability of nonlinear absorption increases strongly with laser intensity [16].

If the carrier density in the conduction band is sufficient, some free carriers can acquire enough energy to create additional conduction band electrons by (*d*) impact ionization. A highly excited electron in the conduction band (higher than the band gap energy) relaxes by releasing part of its energy through promoting another electron from the valence band to the conduction band (impact ionization). This process increases the number of free carriers in the conduction band. If the laser intensity is high enough, multi-photon absorption and impact ionization can lead to optical breakdown, which produces a plasma. [17]



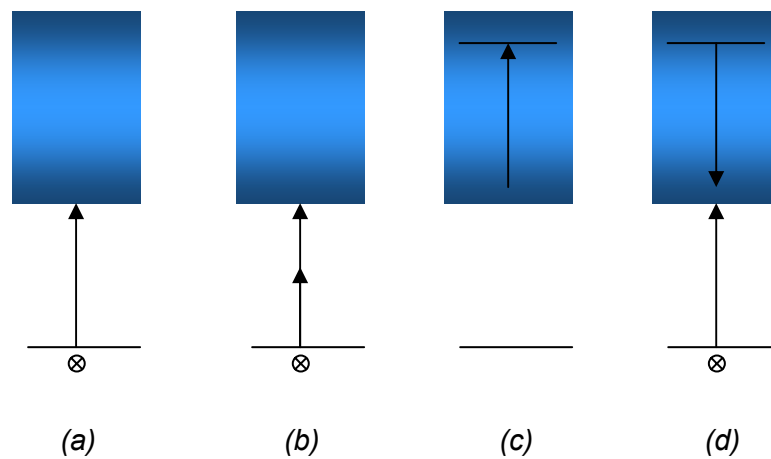*(a)*              *(b)*              *(c)*              *(d)*

Figure 3.1- Schematic of electronic excitation in a semiconductor by laser pulses: (a) single-photon excitation, (b) multi-photon excitation, (c) free carrier-absorption, (d) impact ionization

### 3.2.2 Secondary Processes

The initial electronic excitation is followed by a complex hierarchy of secondary processes. The excited electrons relax and the deposited energy is redistributed through a number of processes which eventually end in the final

structural modification of the material. The time scales of this chain of events can be crudely classified as shown in Fig.3.2 [16]
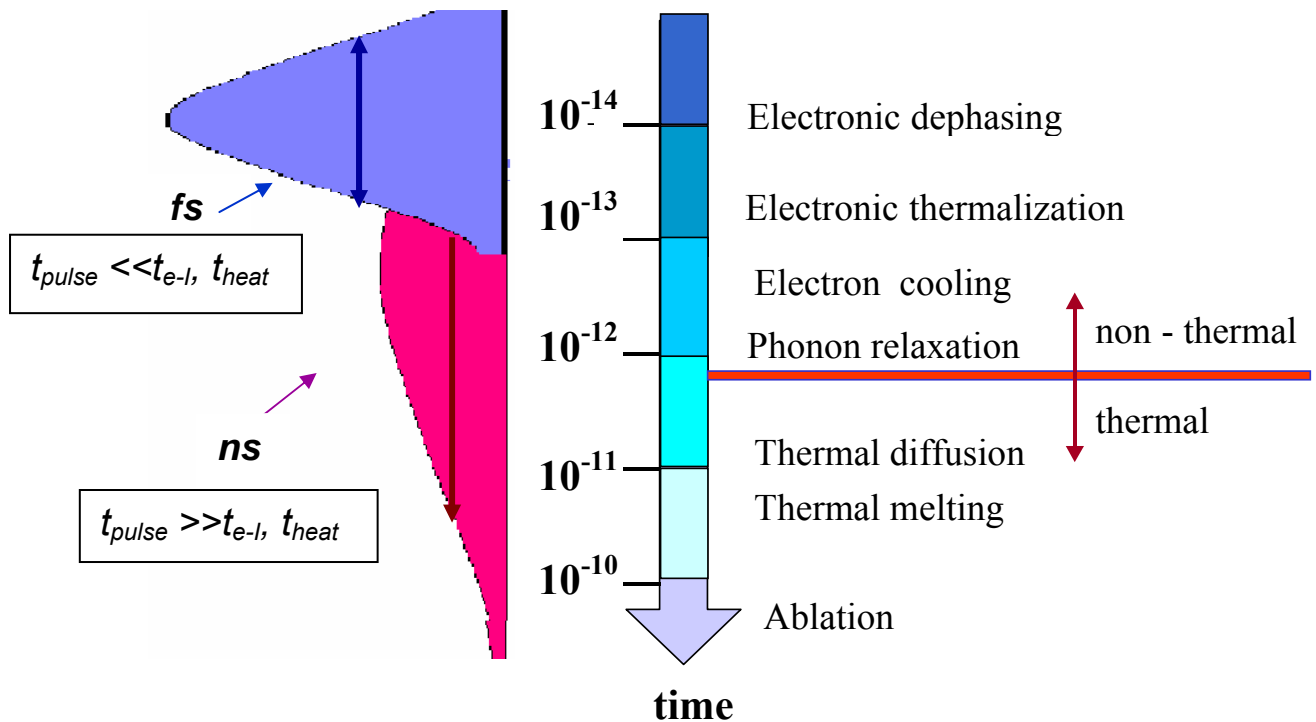


Figure 3.2- Timescales of the various secondary processes- in comparison to the pulse duration at FWHM in the case of ns and fs pulses.

The primary electronic excitation is associated with very short-lived coherent polarization of the material. Dephasing processes destroy the polarization roughly on a time scale of about $10^{-14}$ sec [18]. The initial distribution of excited electronic states is rapidly changed by carrier-carrier interaction processes, and a quasi-equilibrium situation is established among the electrons on a time scale of about $10^{-13}$ sec. The quasi-equilibrium electrons cool down on a timescale of $10^{-13}$ to $10^{-12}$ sec by emission of phonons (carrier-phonon scattering).

The final stage of the thermalization process is the redistribution of the phonons over the entire Brillouin zone according to a Bose-Enstein distribution. At this point the temperature of the laser excited material can be defined, and the energy

distribution is characterized by the temperature. Subsequent processes are of thermal nature. After phonon relaxation and phonon redistribution, the diffusion of heat from the surface to the bulk, follows on the time scale of $10^{-11}$s. If the laser pulse intensity exceeds the melting threshold, melting occurs. Finally, thermal ablation takes place on a timescale of $10^{-10}$s.

There is a distinct dividing line at about $10^{-12}$ s separating the regime of non-thermal processes and thermal processes. Mechanisms leading to structural modifications using picosecond and longer laser pulses are in most cases thermal, i.e., they take place on timescales longer than a picosecond. On the other hand, employment of ultrashort (femtosecond) pulses leads to a different kind of modification. As illustrated in Figure 3.2, when the pulse duration is significantly less than electron-to-lattice (ions) energy transfer time (and subsequently to the heat conduction time), nonthermal pathways may be accessed that take place on a timescale shorter than a picosecond, hence before thermal processes kick in However, there are still aspects of  femtosecond laser induced modification of solids to be interpreted.

### 3.3.3 Macroscopic Consideration

This section examines, from a macroscopic point of view, the effects caused on a solid surface upon intense laser irradiation. On this basis a first order qualitative analysis is extracted. Laser-matter interactions (in a non-reactive surrounding medium) are dependent on the laser parameters (i.e. wavelength, pulse duration, beam energy spatial distribution, etc.) as well as on the thermodynamic properties of the material employed.

Figure 3.2 illustrates light absorption and sample heating in the case when the optical penetration depth is much smaller than the thermal diffusion length [i].

---

[i] This scenario is not indicative of the processes operative in all kinds of materials. This approach is mostly applicable for metals.
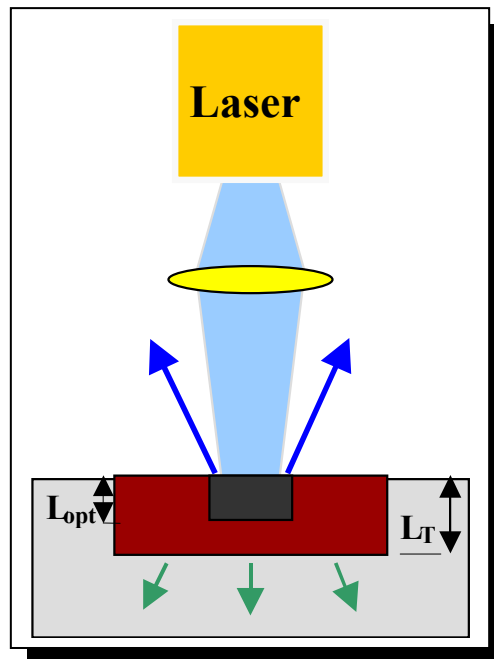
Figure 3.3- Schematic of light absorption and sample heating in the case when $L_{th}$ >> $\alpha^{-1}$. At the end of the laser pulse the deposited heat is approximately confined to the region within the red marked area.

Upon illumination of a solid surface, laser irradiation is absorbed within an area defined by the so-called optical penetration depth (black marked area-Fig. 3.3). This is inversely equal to the wavelenght-dependent absorption coefficient α, as defined in the Beer-Lambert expression (Eq. 3.1).

$$I = I_o \, e^{-\alpha x} \qquad\qquad (Eq.\ 3.1)$$

$$L_{opt} = a^{-1} \qquad\qquad (Eq.\ 3.2)$$

or  alternatively

$$L_{opt} = \frac{\lambda}{2 \cdot \pi \cdot \kappa} \qquad\qquad (Eq.\ 3.3)$$

λ being the laser wavelength and κ being the extinction coefficient.

As noted in the previous section, laser–solid interactions may cause thermal effects. The heat generated at the target surface during a laser pulse of duration τ will be confined to a depth roughly the dimensions of a thermal diffusion length [ii] [19] (red marked area – Fig. 3.3).

$$L_{th} = \sqrt{2 \cdot D_{th} \cdot \tau}$$ 

*(Eq. 3.4)*

where $D_{th}$ is thermal diffusivity given by

$$D_{th} = \frac{K}{\rho \cdot C_v}$$ 

*(Eq. 3.5)*

where ρ is the target density, $C_v$ the specific heat, K the thermal conductivity. Consequently it is clear that lager pulse durations favor thermal diffusion effects. Summarizing the above, we find the optical penetration depth to be a function of the laser wavelength (Eq. 3.3), whereas the thermal diffusion length to be strongly dependant on pulse duration (Eq. 3.4).


## 3.3 LASER INDUCED PERIODIC SURFACE STRUCTURES

A form of laser induced surface modification which appears to be spatially periodic in nature, and which occurs on a wide variety of both opaque and transparent materials, are the so called Laser-Induced Periodic Surface Structures (LIPSS) [20]. Birnbaum [21] was the first to report this gratinglike damage that occurred on the surface of various semiconducting materials, which were used as Q-switching elements in a pulsed ruby-laser system. Since then, similar patterns have been produced in many semiconductors [22,23], metals [24,25], and dielectrics [26,27] using many different continuous and pulsed laser sources. The common characteristics observed on both solids and liquids [28] lead to the conclusion that laser-induced periodic surface structures (LIPSS) by single laser

---

[ii] This is a one dimensional model description which does not consider isotropical diffusion of heat.

beams is a universal phenomenon that can occur on any material that absorbs radiation, regardless of its dielectric constant [32].

Structures that develop on solid or liquid surfaces under the action of laser light can be classified into coherent structures and non-coherent structures [29]. Coherent structures are directly related to the coherence, the wavelength and the polarization of the laser light. These structures have a common origin: the oscillating radiation field on the material surface, which is generated by the interference between the incident laser beam and scattered/excited surface waves. The spatial periods of such structures are therefore proportional to the laser wavelength, while their orientation is perpendicular to the electric vector of the incident light.

Non-coherent structures however, are not directly related to any spatial periodicity of the energy input caused by interference phenomena. Their period is not related to the laser wavelength and polarization. It is related however to the laser-beam intensity and the ambient gas pressure, when such is used [29].

According to Young et. al [32] LIPSS's spatial period is related to laser intensity and a classification in to fluence regimes may be considered on this basis. At relatively low fluences (low fluence regime) [32, 30] fine periodic microstructures having a characteristic wavelength may evolve as the number of pulses on a given region is sequentially increased. At higher fluences (high fluence regime) however, a wave-like topography with wavelength much larger than the incident laser wavelength has been observed [31]. The formation of these periodic structures has often been related to capillary waves [34].

### 3.3.1 Capillary Waves

Capillary waves can be generated at the air/liquid-Si interface at elevated fluences. If the decay of the capillary-wave activity is not complete by the time the surface resolidifies, a permanent record of the ripples is "frozen" into the surface [32].

It is well known that if the wavelength of a perturbation at a liquid surface is much less than $(a/\rho g)^{1/2}$, the dominant restoring force is provided by surface

tension. The dispersion of the natural oscillation frequency $\omega_c$ for shallow capillary waves is given by the following expression [33].

$$\omega_c = \left( \frac{a \cdot h}{\rho} \right)^{\frac{1}{2}} \cdot \kappa_c^{\,2} \qquad\qquad (Eq.\ 3.6)$$

where a is the surface-tension coefficient of the air/liquid interface, $\rho$ is the density of the liquid, h is the thickness of the liquid and $\kappa_c$ is the wave vector of the surface perturbation while

$$\kappa_c = 2\pi/\lambda_c, \qquad\qquad (Eq.\ 3.7)$$

where $\lambda_c$ is the wavelength of the capillary wave.

Alternatively the wavelength of the capillary wave may be given by Eq. 3.8

$$\lambda_c = \left[ \frac{\alpha \cdot h}{\rho} \right]^{1/4} \cdot \left( 2 \cdot \pi \cdot \tau_c \right)^{1/2} \qquad\qquad (Eq.\ 3.8)$$

where $\tau_c$ is the period of the capillary wave.

Viscous forces cause the amplitude A of the capillary waves to decay as:

$$A \sim e^{-\gamma t}, \qquad\qquad (Eq.\ 3.9)$$

where

$$\gamma = (2\eta/\rho)\kappa^2 = 2\nu\kappa^2. \qquad\qquad (Eq.\ 3.10)$$

Here, $\eta$ is the shear viscosity and $\nu$ is the kinematic viscosity of the liquid [32].

The origin of the capillary waves may be attributed to a spatially stable and periodically non-homogeneous deposition of energy driving the motion of liquid from the hotter regions into the colder regions by a gradient of surface tension [34], deforming the surface. Relaxation of the deformation as the molten Si cools can then excite capillary waves in the molten Si [35]. The key element in all the capillary processes is that the liquid moves so as to increase the amplitude of the wave. This implies that there are surface or volume forces acting on the liquid that oppose the tendency of a liquid wetting its own solid to decrease the surface energy by decreasing the surface area.

In the case when there is a non-homogeneous energy deposition, another possibility for the creation of a wave-like surface topography is the removal of material by preferential etching and ablation at the hotter spots. The formation of

this long period wave-like pattern can be due to a combination of both the effects just mentioned [34].

However the formation of the coarsened layer and subsequent fragmentation into microspikes could also involve plasma oscillation induced by the trailing edge of the light pulse [35]. A resonant interaction between the plasma and the laser pulse light occurs when the plasma frequency equals the laser light frequency [36]. This resonance occurs because the electron density increases with increasing laser fluence: the corresponding plasma frequency can therefore increase until the plasma frequency is resonant with the laser light frequency and the electromagnetic field couples directly to the plasma oscillation. However it is shown, that increasing the laser fluence both the typical separation of the microspikes and wavelength of the coarsened layer increases [35]. If the microspike separation was determined by the plasmon wavelength, increasing the plasma density, and therefore the plasma frequency should instead decrease the typical separation of the microspikes and the wavelength of the coarsened layer. Therefore plasma oscillations cannot be responsible for the arrangement of the microspikes.

.

## 3.4 LASER INDUCED SI MICROCOLUMN ARRAYS

The potential of fabricating Si based microtip array field emitters, as discussed in Chapter 2, appears to be quite intriguing. Moreover the possibility of fabricating Si microtip arrays utilizing laser pulses opens up a whole new prospective for cold cathode field emitter manufacturing technology.

Attempts to provide a consistent interpretation of the mechanisms of Si spikes formation in reactive gas atmospheres have been performed by several groups [37, 42, 38]. Spikes growth has been attributed to the combinative operation of laser-solid interaction and laser-assisted chemical etching. The next section will review the mechanisms of Si microstructures formation, i.e. how they evolve from a starting wave-like inhomogeneity (i.e. capillary waves) and how they grow and

become more pronounced in a reactive gas environment ($SF_6$). A more detailed categorization of the possible interaction mechanisms in terms of laser pulse duration will is given in Chapter 6.

### 3.4.1 Si Spikes Growth Mechanisms

Growth of spikes due to laser-solid interaction is interpreted on the basis of preferential material removal. The surface waves (i.e. capillary waves) serve as the starting inhomogeneity of the absorptivity of the surface. The formation of elongated cone-like structures is possible owing to the increase of reflectivity of the surface with the increase of the incident angle [37][38]. This results in material removal mostly in those areas of the wafer that are oriented to the normal of the laser beam axis, that is between the cones. This variation of the reflectivity provides the preservation of the conical structure at laser fluence close to the threshold of melting.
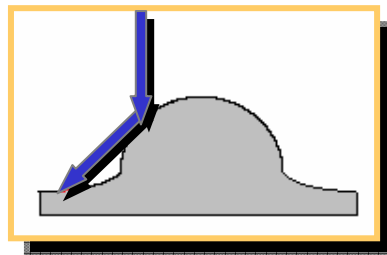


Fig.3.4- Schematic of light reflection off a protrusion leading to enhanced light absorption in the intercone areas.

Moreover laser irradiation is reflected from the cones to the valleys between them. This leads to irradiation trapping in the intercone areas, where the local laser fluence is sequentially increased (Figure 3.4).

### 3.4.2 Laser Induced Chemical Etching

Laser chemical processing of materials is a means of material modification inducing either an overall change in the chemical composition of the material or the activation of a real chemical reaction [29]. Alternatively, photochemical etching of semiconductors is based on the interaction between radicals and carriers

within the semiconductor surface. Radicals can be formed spontaneously by molecule-surface interactions, by selective electronic excitation, or by vibrational excitation of the etchant.

The photochemical etch rates sequentially depend on the concentration of the active species within the ambient medium, on the optical penetration depth of the laser light in the semiconductor surface, carrier lifetimes, recombination processes etc. One of the most extensively used gases for etching of semiconductors, and in particular Si with which it is very active, is $SF_6$.

**Si-$SF_6$ Interaction**

At room temperature $SF_6$ is stable and does not chemisorb on Si. However heating at approximately 1000 $^o$C may initiate a thermal reaction. This suggests that laser heating could cause a reaction. $SF_6$ can be physisorbed at 90K or for $P \geq 1$Torr at room temperature [29].

$SF_6$ dissociation is well known in plasma etching applications. This dissociation led to the formation of fluorine radicals using either radio frequency discharge chamber or electron beam.

Laser induced etching of Si with $SF_6$ can take place via a vibrationally or electronically excited molecule or a radical created by photodissociation. The course of the latter interaction has been studied using $CO_2$ laser pulses in the presence of $SF_6$ at normal incidence to the Si substrate. Vibrationally excited $SF_6$ is very reactive with Si. The dominant volatile products of this reaction are $SF_4$ and $SiF_4$. It has been suggested that gaseous or physisorbed $SF_6$ molecules are excited into higher vibrational states via coherent multiphoton excitation. In contrast to ground-state $SF_6$, vibrationally excited $SF_6$ can dissociatevely chemisorb on Si surfaces resulting to the formation of fluorine ions and the volatile $SF_4$. Part of the chemisorbed $F^-$ ions penetrate into the Si forming a fluorosilyl layer. Via a number of subsequent processes $SiF_4$ is formed and desorbs from the surface [29].

With very high fluences and parallel incidence of the $CO_2$ irradiation, decomposition of $SF_6$ may occur due to coherent and multiphoton absorption (via the vibrational state ladder) resulting in its dissociation. $SF_6$ molecules decompose

into $SF_5$ and F atoms. $SF_5$ (being very unstable) decomposes into $SF_4$ and another F atom, which both diffuse into the Si surface and react to form $SiF_4$.

Pedraza et al [42] have suggested that fluoride compounds such as $SiF_2$ and $SiF_4$ which are volatile at the transient temperatures reached during laser heating are formed under irradiation with a KrF ($\lambda$=248 nm, $\tau$=25 ns) excimer laser. $SiF_2$ reacts with Si to produce $SF_4$ and F.

A more extensive interpretation of the interaction of the high intensity pulses employed for this set of experiments with $SF_6$ and the processes operative, leading to Si etching are given in Chapter 6.


## 3.5 PREVIOUS STUDIES ON LASER INDUCED SI SPIKES FORMATION

Si spikes formation has been examined over the past few years, with the use of several laser sources, including both ns and fs pulses in the presence of various inert gases. The formation of whiskerlike periodic structures in air, using an ArF ($\lambda$=193nm, $\tau_{FWHM}$=23 ns) excimer laser has been investigated by Sanchez et al [39][40]. The structures obtained with the laser energy density varying ranging from 1,5 to 2.5 $J/cm^2$ were up to 20-30 $\mu$m high with a tip diameter of 1-2 $\mu$m. More recently the formation of elongated structures on silicon as well as the dynamics of their growth were investigated by Pedraza et al. [41, 42]. Micro-columns 20-40 $\mu$m high and with a tip diameter of 2-3 $\mu$m that protruded above the initial surface were obtained with the use of a KrF ($\lambda$=248 nm, $\tau_{FWHM}$=25 ns) excimer laser. Microstructuring in this case took place in the presence of $SF_6$ while the laser energy density ranged between 2.7-3.3 $J/cm^2$.

Silicon microstructuring with fs laser pulses has been reported by Her et al. [43, 44]. Silicon surfaces developed an array of sharp conical spikes when irradiated with laser pulses of a Ti:sapphire ($\lambda$=800 nm, $\tau_{FWHM}$=100 fs) laser system with a laser energy density of 1$J/cm^2$. Experiments took place in the presence of 500 Torr $SF_6$ or $Cl_2$. The spikes formed in $SF_6$ were up to 40 $\mu$m tall while they are capped by a 1,5 $\mu$m ball on their top. An interesting feature was the fact that these structures were formed below (did not protrude above) the original surface.

Additionally, the spikes separation was much larger than the laser wavelength and they exhibited higher density at the outer part of the laser spot.

Recently Karabutov et al. [45] have reported field emission measurements on microstructured silicon samples by a Cu vapor laser (510.6nm, 20ns). Silicon spikes were obtained in the presence of nitrogen or at a residual air pressure of 1Pa. The samples were dipped in $HF/H_2O/C_2H_5OH$ solution after the laser irradiation. Their tip radius was about 1-2μm while their height ranged from 10 to 30μm. The best samples showed emission at threshold fields as low as 4-5 V/μm for n-type Si and 1-2 V/μm for p-type Si measured.

The field emission of electrons from laser produced silicon tip arrays obtained with the use of a Nd:YAG ($\lambda$=1.06μm, $\tau$=0.2ms) laser in air has also been studied [46]. The silicon tip array with distance between tips of approximately 50 μm, height of 50-100 μm, with a radius of top of about 1μm was produced with a laser energy density of 0.2 J/cm$^2$. The field emission was obtained from nanocomposite structures in the drive voltage range from 100 to 1500V and in the current range from 5nA to above 20 μA in air.

Moreover, recent interest has been placed on the fabrication of ordered arrays of silicon cones by optical diffraction in ultrafast laser etching with SF$_6$ [47]. This work puts into evidence the prospective of spatially (in one dimension) controlling the location of the structures via near-field diffraction of the incident beam.

In the present work, the field emission properties results from self-organized Si micro-tips produced by laser ablation of n-type Si wafers were examined. A systematic study of different laser sources has been performed and emphasis was given on the optimisation of silicon spikes formation conditions (laser and ambient gas pressure parameters) on the basis of homogeneity and aspect ratio maximization, in a controlled and reproducible manner. Experimental results are given in Chapter 5.

# CHAPTER 4

## EXPERIMENTAL PROCEDURE

## 4.1 INTRODUCTION

This chapter includes a description of the experimental apparatus employed for the purposes of this work. Furthermore it presents the characterization techniques and instrumentation for obtaining a morphological characterization. Finally the setup for field emission measurements is presented briefly.

## 4.2 LASER SOURCES

The laser sources employed for this set of experiments were:

- A Lambda Physik EMG 201MSC XeCl excimer laser ($\lambda=308nm$, $\tau_{FWHM}=32ns$)
- A distributed-feedback dye-laser based KrF fs excimer laser system ($\lambda=248nm$, $\tau_{FWHM}=500fs$)
- A regenerative amplified Ti:Sapphire laser system ($\lambda=800nm$, $\tau_{FWHM}=50fs$)

### 4.2.1 The sub –picosecond KrF excimer laser system

Sub-picosecond laser pulses are obtained from a hybrid excimer-dye laser system based on the concept of the distributed feedback dye laser (DFDL). In order to obtain these pulses a complicated arrangement is employed [48],[49]. The output of a double-cavity excimer laser (Lambda Physik EMG 150MSC) excimer laser (at 308 nm) is used as a pump laser for a special sub-picosecond dye laser amplifier system, and as an amplifier (at 248 nm) for the frequency-doubled output pulses of the dye laser set-up. Part of the output of the XeCl laser is used to pump a Distributed Feedback Dye Laser (DFDL), which in turn generates the pumping laser beam for the KrF laser cavity. This pump source consists of two dye lasers, two amplifier stages and a gated saturable absorber (GSA) placed between the amplifiers. The resulting output pulse has a duration of a few ps,

while being centred at 365 nm, and is used for pumping the DFDL which allows the generation of short, femtosecond pulses from a seeding pulse of longer duration. The output wavelength of the DFDL is set to twice the KrF wavelength (496 nm), and is sequentially amplified via a two-stage amplifier, separated by a saturable absorber and frequency doubled by a Beta-Barium Borate (BBO) crystal to yield pico-second seeding pulses of 248 nm wavelength. This seeding pulse is amplified through a KrF excimer laser, via a double pass arrangement shown in Fig. 4.1, yielding pulse energies up to 10mJ with pulse length of 500 fs. 5 ps laser pulses can also be generated by insertion of a multiple reflection etalon in the dye laser set-up.



Fig. 4.1- Schematic of the set-up of a sub-ps excimer laser

### 4.2.2 The femtosecond Ti:Sapphire laser system

The ultrafast laser system employed in this experiment, comprises a commercial Coherent/B.M. Industries system, utilizing a combination of a MIRA oscillator and a kHz two stage amplification configuration.

The oscillator which is based on a Ti:Sapphire, Kerr lens mode locking configuration, is pumped by a CW diode laser (VERDI COHERENT) and generates pulses of 25 fs at 800 nm, having a pulse energy of 5 nJ.

Before seeding the amplification stages, the generated pulses, are stretched up to 1000-5000 times their initial temporal duration in order to prevent optical damage which may arise because of the extremely high intensity.

The first amplification stage comprises a so called regenerative amplifier, where selected pulses are trapped in, using Pockels Cell based polarization switching. The active medium of the regenerative amplifier is a Ti:Sapphire pumped by a doubled Nd:YLF laser (532 nm) at 10 W. The amplifier outputs pulses with 1.5 mJ/ pulse at 1 kHz repetition rate.

The second amplification stage is based on a multi-pass amplifier configuration, where the pulses are amplified up to ~4mJ, again using Ti:Sapphire as an active medium. Finally, the pulses are compressed by a grating-pair compressor in to 40 fs duration, having energy of 2.5 mJ/ pulse.
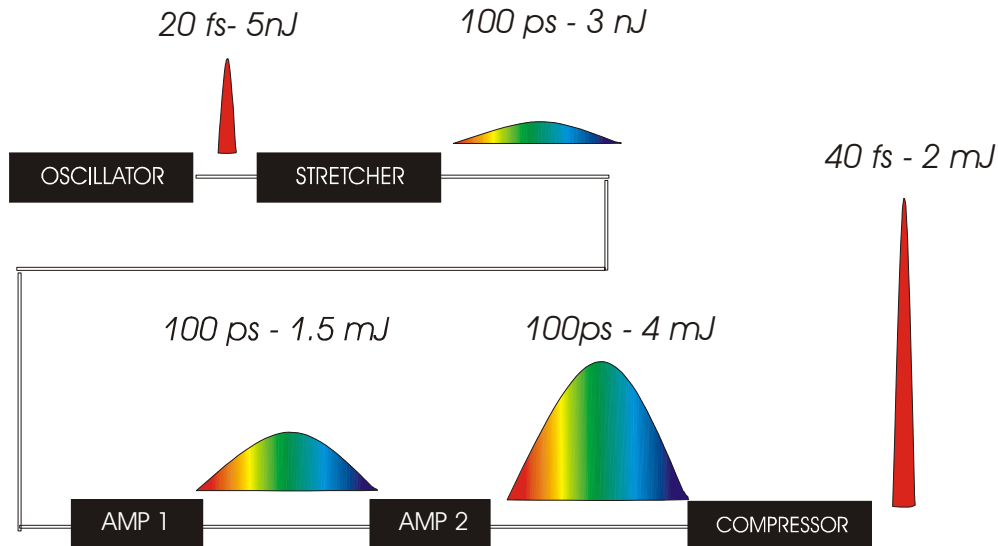


Fig. 4.1- Pulse evolution through the amplification stages

## *4.2.3 Laser Beam Spatial Energy Distribution*

In the course of this work it was found that the quality of the laser beam was of prime importance for the results obtained. To this effect detailed measurements of the laser beam energy distribution were performed

### 4.2.3-1 XeCl Excimer Laser Beam Characterization

The laser beam in this case was diagnosed by means of an ICCD camera configuration. The beam was focused in the camera aperture via a spherical lens while attenuators the filters were employed for preventing damage due to the high intensity. Here at the beam profile at 16kV discharge voltage is illustrated.



(a)                                          (b)
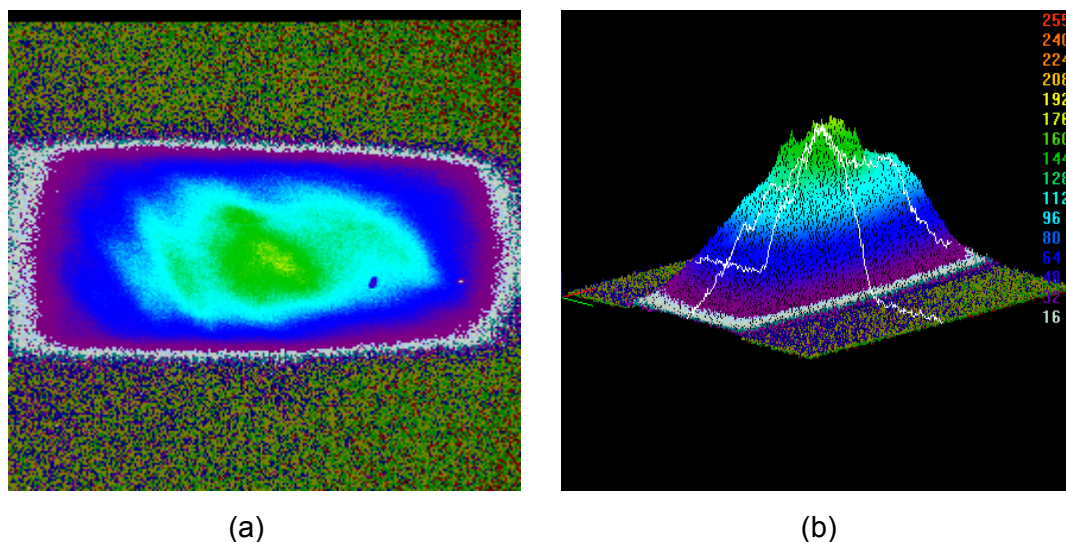
Fig. 4.3- XeCl ns eximer laser beam energy spatial distribution in (a)2-dimensions and (b) 3-dimensions

The above image shows a relatively smooth curved beam profile top. However an evident striping feature appears when the beam is more intensely focused.

### 4.2.3-2 KrF Excimer Laser Beam Characterization

Using a similar configuration as described in section 4.2.3-1 the beam profile of the sub-ps KrF excimer laser was recorded.
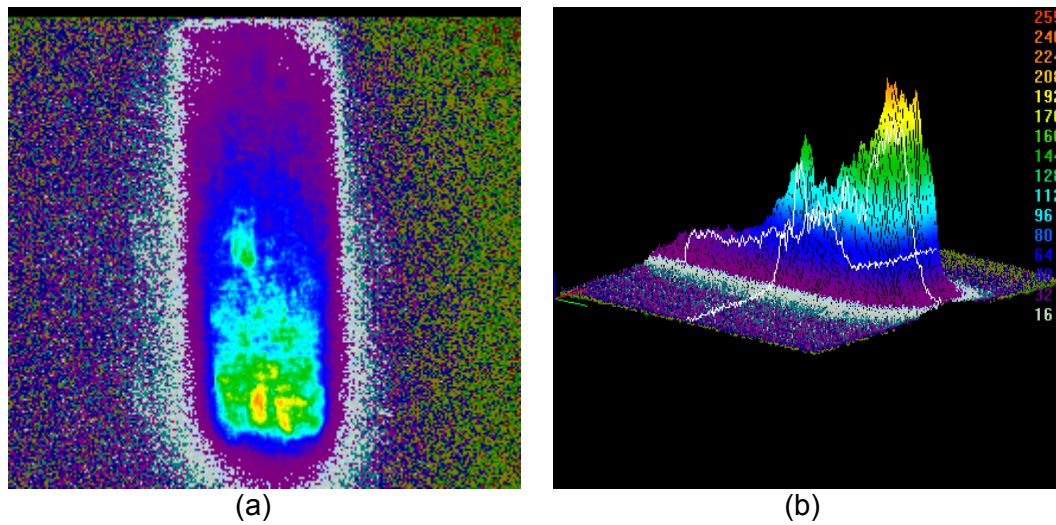
Fig. 4.4- KrF sub-ps laser beam energy spatial distribution in (a)2-dimensions and (b) 3-dimensions

As it is clearly seen that there is an inhomogeneous beam energy spatial distribution. Energy is concentrated on the upper area of the laser spot, where the beam profile top appears to be particularly rough with existing spiking peaks.

### 4.2.3-1 Ti: Sapphire Laser Beam Characterization

The Ti:Sapphire laser beam was characterized using the scanning knife edge method. This technique utilizes a sharp object scanned across the laser beam axis. The variation of the total power of the laser beam transmitted through can give information about its spatial energy distribution.

A razor edge is used as knife edge and mounted on a translation stage with a micron scale resolution allowing the edge scanning across the laser beam axis with a 100μm step size. In a step-by-step fashion, the knife edge is scanned across the laser beam and the total transmitted power was recorded.

Through this process, additional information concerning In this manner the radius of the focused beam may be estimated through Equation 4.1

$$\mathrm{w}_f = \frac{\lambda f}{\pi w_s} \tag{4.1}$$

$$\mathrm{w}_s = 0.7803 \Delta d \tag{4.2}$$

where ($\lambda$) is the wavelength, (f) the focal length of the focusing object and ($w_s$) the radius of the laser beam at the location of the focusing object. $\Delta d$ is the distance between 90% and 10% of the transmitted maximum laser beam power.

Figure 4.5(a) and (b) illustrate the beam profile after a scan across the x- and y-axis respectively
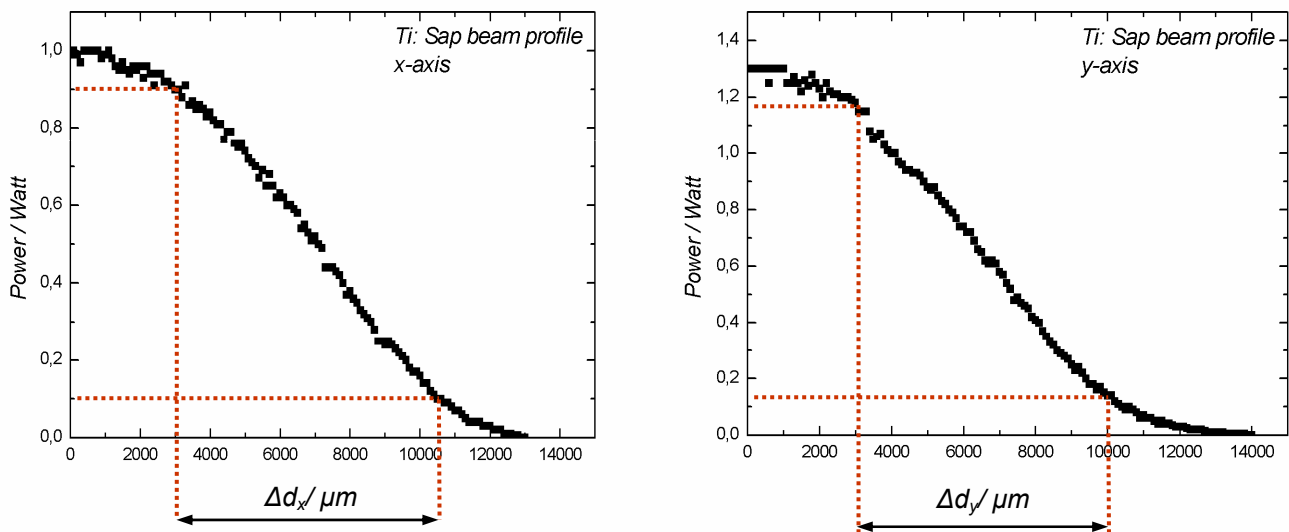


Figure 4.5- Ti:Sapphire beam power profile in (a) x-direction and (b) y-direction, measured with the scanning knife edge method. The radius of the laser beam is distinguished with $w_s$ = 0.7803$\Delta d$, where $\Delta d$ is the distance between 90% and 10% of the transmitted maximum laser beam power.

## 4.3 SAMPLE PREPARATION

The samples used for producing the Si microtip arrays were 10mm x 10mm squares cut from 3- or 4- inch commercial single crystal n-type [iii] (phosphorous-doped) Si wafers. Their crystallographic orientation was (100) while their resistivity ranged between 2-8 Ohm·cm.. The samples were cleaned in an ultrasonic acetone bath prior to irradiation.

---

[iii] n-type Si prompts a shift of the Fermi energy closer to the conduction band. Accordingly a lower applied field is required to commerce field emission.

## 4.4 EXPERIMENTAL SETUP

Silicon microstructuring took place in a vacuum chamber evacuated down to a residual pressure of ~$10^{-2}$ mbar by means of a rotary pump. The background pressure was measured using a pirani gauge. A micro valve system attached to the chamber enabled a precise backfilling of a halogen-containing ambient gas ($SF_6$). The pressure of the backfilling gas was measured with a baratron gauge.

The chamber was placed on a computer driven high precision X-Y translation stage with spatial resolution of 1 μm allowing sample displacement with regard to the laser beam up to 100 mm. This system allowed control over the amount of overlap between consecutive scans when large area microstructuring was required.

The laser beam in most cases was shaped by an iris and was focused with a quartz lens on to the sample, which was mounted on a sample holder inside the vacuum processing chamber. The laser fluence was varied by using filters or attenuators. The laser beam entered the chamber through a quartz entrance window, while the irradiation process could be observed optically through a plexiglas window, which was laterally mounted at the vacuum chamber.

Minor variations of the experimental setup were performed from laser source to the other, regarding the optical configuration and means of laser triggering. For the KrF as well as for the XeCl laser source the number of incoming pulses as well as the delay were dictated by sychronizing the laser to the translation stages. However for the Ti:Sapphire laser source operating at a repetiton rate of 1 kHz, where direct triggering from the laser could not be accomplished, a mechanical shutter synchronized to the computer driven translation stages was employed (as may be seen in Fig. 4.6), allowing to direct laser pulse packages into the processing chamber.
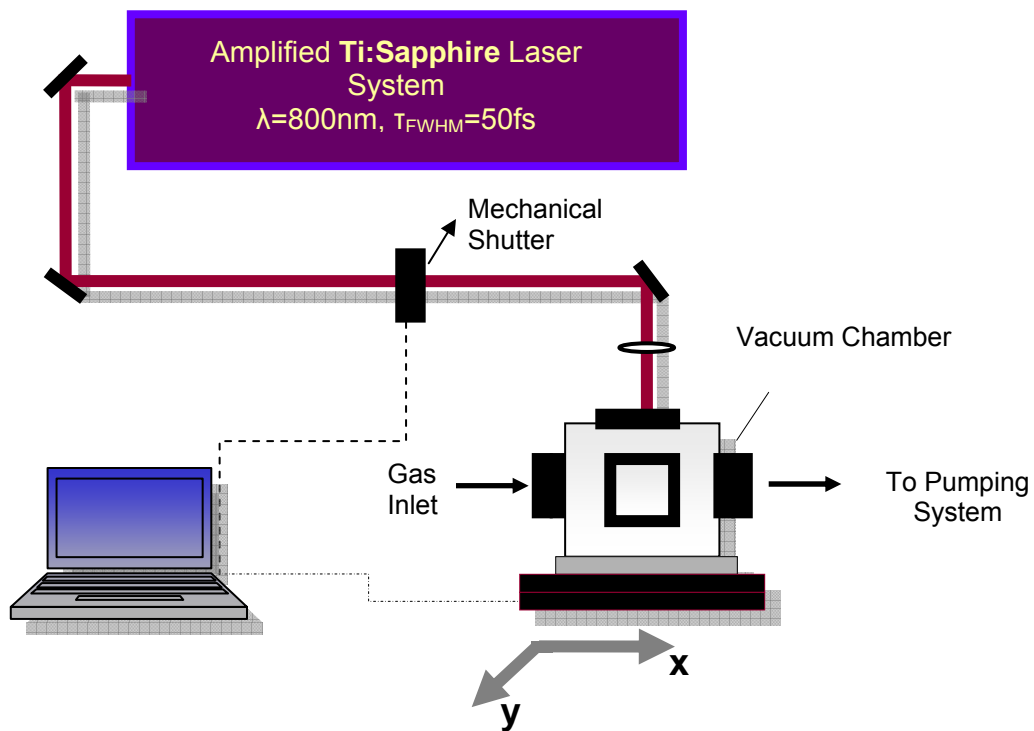
Figure 4.6- Experimental Setup

## 4.5 SAMPLE CHARACTERIZATION

### 4.5.1 Scanning Electron Microscopy

The sample characterized is irradiated with a finely focused electron beam, which is swept in a raster across its surface. The types of signals produced when the electron beam impinges on a specimen surface include secondary electrons, backscattered electrons, Auger electrons, characteristic x-ray, and photons of various energies [Fig. 4.7]. Signals by the secondary and backscattered electrons are obtained from specific emission volumes within the sample and can be used to examine the sample surface topography.
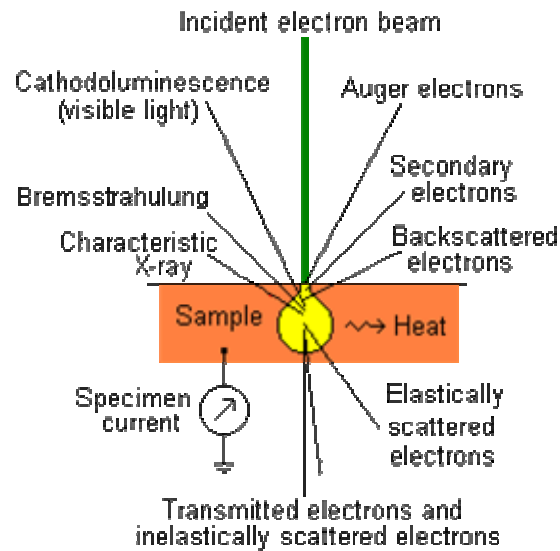
Figure 4.7-Types of signals produced when the electron beam impinges on a specimen surface

The primary (exciting) electron may interact with an electron in the sample, ejecting it with some amount of kinetic energy. If the ejected electron is weakly bound, it typically emerges with only a few eV of energy and is called a secondary electron. Secondary electrons can escape from the sample to be detected only if they are created near the surface, since they have little energy. The secondary electron emission is confined to a volume near the beam impact area, permitting images to be obtained at relatively high resolution. The three dimensional appearance of the images is due to the large depth of field of the SEM as well as to the shadow relief effect of the secondary electron contrast.

### 4.5.2 Field emission testing

$2x2mm^2$ areas of $n^+$ Si targets were tested as cold cathode field emitters. Field emission measurements were performed in vacuum ($< 10^{-6}$ mbar) in a planar configuration with the produced sample used as the cathode and collecting the emitted electrons on an ITO anode with effective area of $0.25cm^2$. The electrode spacing was 200 μm defined using a Teflon spacer. The emitted current was recorded during the increase and decrease of the applied voltage.
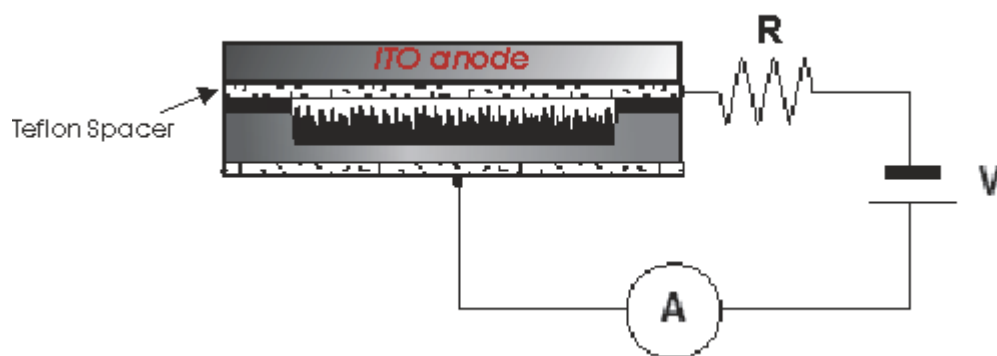
Figure 4.8- *Apparatus used to measure field emission from Si microstructures*

# CHAPTER 5

## RESULTS & DISCUSSION

## 5.1 INTRODUCTION

This chapter exhibits the experimental results obtained in the course of this work. The morphological characterization of the structures obtained was achieved by means of an SEM allowing the different stages of spikes evolution to be studied in detail. The influence of laser as well as ambient gas ($SF_6$) parameters on the quality of the obtained structures was examined and their contribution in defining their properties in a controlled and reproducible manner was considered. In particular, a comparative study using nanosecond (ns), sub-picosecond (sub-ps) and femtosecond (fs) laser pulses has been performed. Common trends observed are interpreted, while mechanistic aspects are also discussed.

Moreover the field emission properties of the Si micro-columns were examined, showing that these laser induced structures formed in the presence of a reactive gas show great potential as field emitters.

## 5.2 MORPHOLOGICAL CHARACTERIZATION

The laser-induced periodic structures, indicated as spikes on the bottom of the irradiated spot, are produced without the use of any mask. The observed spikes form spontaneously with varying shape, size, height, morphology and density under different experimental conditions (i.e laser and ambient gas pressure parameters). In all cases the spikes point along the incident laser beam direction. After carrying out single spot irradiation on the surface, it was observed with scanning electron microscope that the distribution, shape and density of the
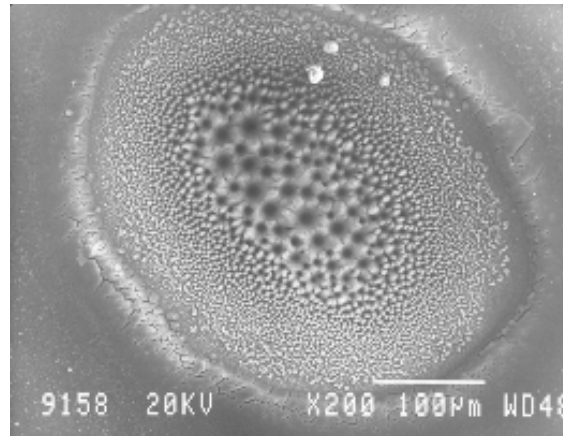
Figure 5.1- Demonstration of the distribution, shape and density of laser induced microspikes on silicon over the laser beam profile. The center of the spot is packed with a low density of tall and wide spikes, while at the edge of the spot small and narrow spikes are packed with a high density. The result is leading to a strong dependence of the forming mechanism on the laser fluence.

microspikes is not homogenous on the induced spot, reflecting the variation of the energy across the Gaussian laser beam profile, which is indicating a strong dependence of the formation mechanism on the laser fluence. In Figure 5.1, the distribution of the spikes on a single spot is demonstrated. The spikes in the center of the laser induced spot are wider, taller and more sparly placed, while the spikes near the edge of the spot are smaller, narrower and packed with a higher density. A periodic ripple structure can be observed at the low fluence part at the edge of the spot. This is in agreement with the theoretical considerations for the low fluence regime for ripple formation as discussed in Chapter 3.

A striking feature observed in our experimental results, is that independently on the laser source employed, the Si surface has a black appearance, when microstructuring has taken place in an $SF_6$ atmosphere. This suggests an increased absorbance of microstructured Si over the visible wavelengths.

### 5.2.1 Experiments with the XeCl ns laser source
This section demonstrates a parametric study examining the influence of:

- Laser fluence,
- Number of laser pulses (i.e. irradiation time),
- Ambient gas pressure ($SF_6$) and

- Laser repetition rate

on the morphology of the obtained Si microcolumns using the XeCl ($\lambda$=308nm, $\tau_{FWHM}$=32ns) excimer laser source

Additional information concerning the height and spike density as a function of parameters like number of pulses and laser fluence respectively will be exhibited. Under the best conditions the obtained spikes had a tip diameter of 2-3μm while their height reached up to 90μm.

## 5.2.1-1 Fluence Dependence

SEM micrographs of the silicon micro-columns obtained by cumulative pulsed laser irradiation of silicon wafers by the XeCl ns excimer laser source are shown in Figure 5.3 [iv]. Spikes evolution was studied upon irradiation with 1000 pulses at a repetition rate of 5 Hz with laser fluence ranging between 1.5 and 4.0 J/cm$^2$. Microstructuring in this case took place in the presence of 500 Torr of $SF_6$, where no spikes were observed for fluences lower than 3 J/cm$^2$. The spikes separation distance increases (thus spikes density decreases) with increasing laser fluence [Fig. 5.2].
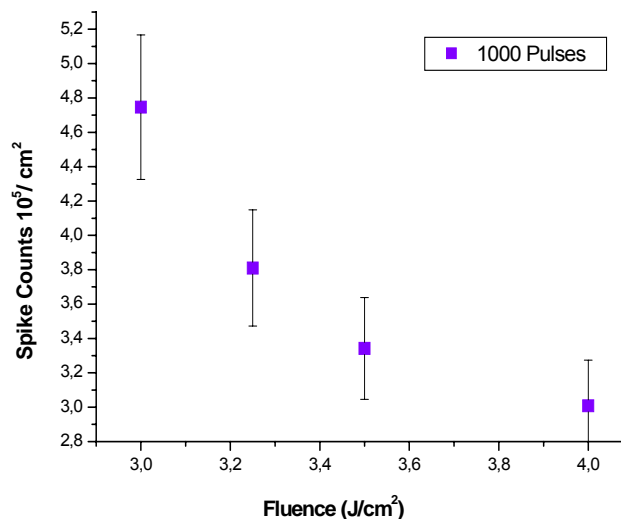


Figure 5.2- Spikes Density (i.e. spike counts / area unit) as a function of laser fluence, for Si spikes obtained using the XeCl (ns) laser source

---

[iv] To avoid any problems associated with fluence variations over the beam profile, we obtain data concerning spikes density by measuring the spikes separation at the center of the laser profile for different fluences.
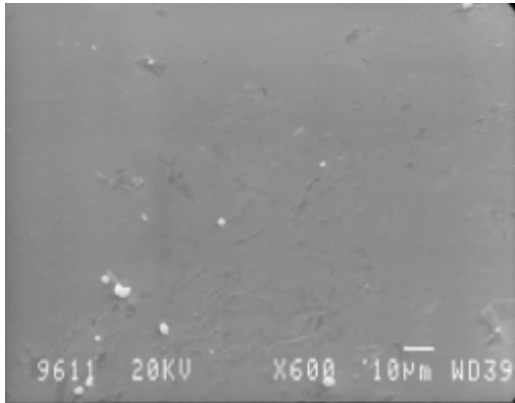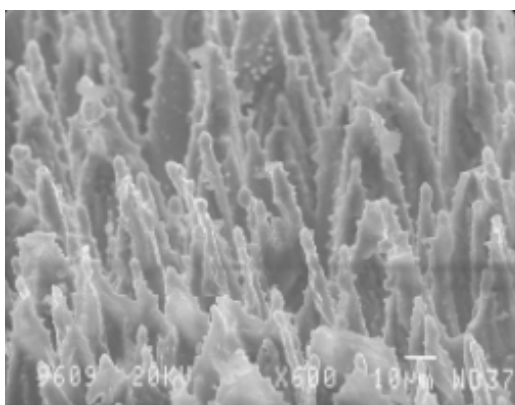
*(a)*
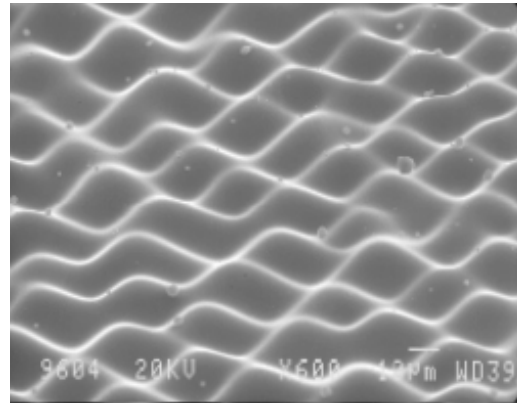


*(b)*
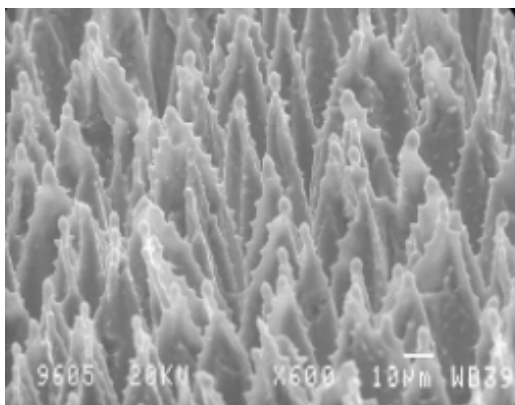


*(c)*
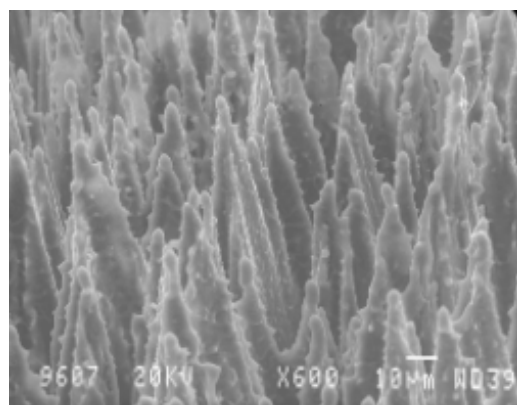


*(d)*



*(e)*

Fig. 5.3- SEM view (45°) of the laser fluence influence on the obtained Si spikes morphology, upon irradiation with 1000pulses of a XeCl ($\lambda$=308nm, $\tau_{FWHM}$=32ns) excimer laser at a fluence of (a) 1,5 J/cm$^2$, (b) 2,0J/cm$^2$, (c) 3,0 J/cm$^2$, (d) 3,5 J/cm$^2$ and (e) 4,0 J/cm$^2$. Microstructuring took place in the presence of 500 Torr SF$_6$. The laser repetition rate was 5 Hz

## 5.2.1-2 Number of Pulses Dependence

Figure 5.5 depicts SEM photographs of the Si spikes obtained for varying number of pulses (100-3000). An evident tendency to a rapid increase in height with increasing number of pulses is observed [Fig 5.5]. This phenomenon appears to be approaching a plateau when an elevated number of pulses (>2000) is applied [Fig.5.4]. The height of the microcolumn structures increases rapidly as the number of pulses increases. The same behavior concerning the growth mechanism has been observed by Pedraza et.al. [50]

Microstructuring in this case took place in the presence of 500 Torr $SF_6$. The laser fluence was 3.5 $J/cm^2$, while the laser repetition rate was set at 5 Hz.
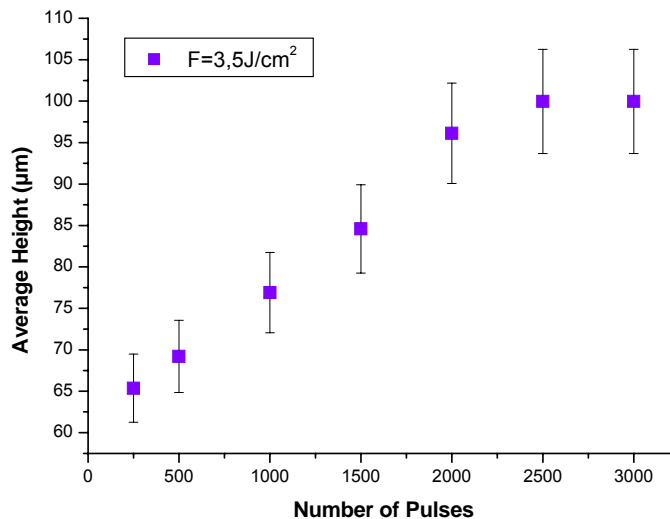


Figure 5.4- Spikes Average Height (in μm) as a function of the Number of Pulses, for Si spikes obtained using the XeCl (ns) laser source.

*(a)*



*(b)*



*(c)*



*(d)*



*(e)*



*(f)*



*(g)*
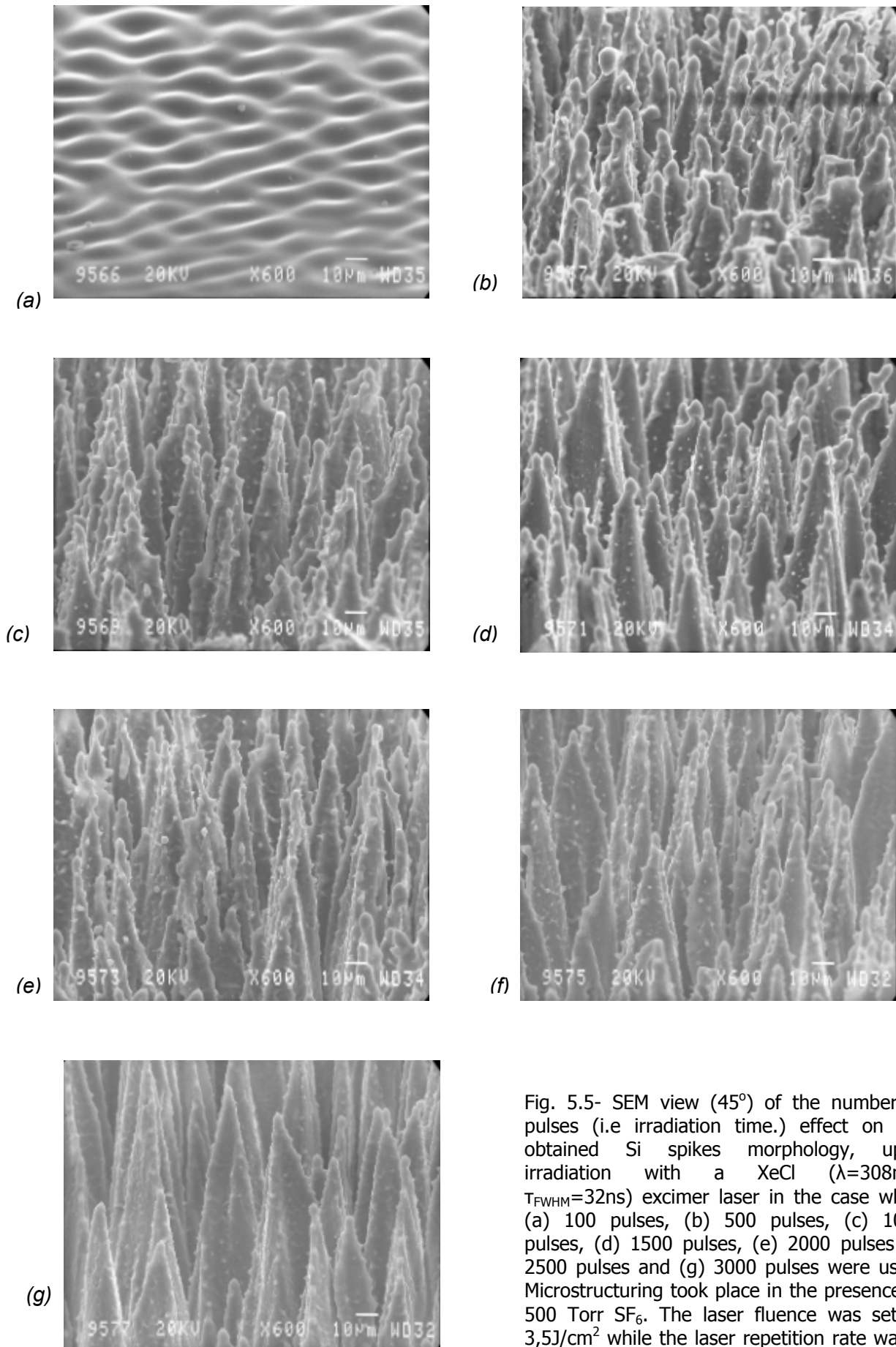
Fig. 5.5- SEM view (45°) of the number of pulses (i.e irradiation time.) effect on the obtained Si spikes morphology, upon irradiation with a XeCl ($\lambda$=308nm, $\tau_{FWHM}$=32ns) excimer laser in the case when (a) 100 pulses, (b) 500 pulses, (c) 1000 pulses, (d) 1500 pulses, (e) 2000 pulses (f) 2500 pulses and (g) 3000 pulses were used. Microstructuring took place in the presence of 500 Torr $SF_6$. The laser fluence was set at 3,5J/cm$^2$ while the laser repetition rate was 5 Hz.

**5.2.1-3 Ambient Gas Pressure Effect**

The formation of silicon spikes both in vacuum and with ranging $SF_6$ pressure (250-1250 Torr) was studied [Fig. 5.6] using the XeCl ns laser source delivering pulses at a repetition rate of 5Hz. Irregular and blunt structures are obtained in vacuum however the tips become sharper with increasing $SF_6$ pressure in the range 250-1250 Torr. The enhanced presence of secondary tip decoration of a few hundred nanometers in diameter with increasing gas pressure was observed. The laser fluence was set at 3.5 $J/cm^2$.

**5.2.1-4 Repetition Rate Influence**

Figure 5.7 shows SEM micrographs of the Si surface upon irradiation with 1000 pulses at a fluence of 3.5 $J/cm^2$ , while the laser repetition rate ranged between 1 and 20 Hz. Appearance of enhanced secondary tip decoration was observed in this case also,  with increasing repetition rate [Fig. 5.7] and was more evident for repetition rates succeeding 10 Hz.
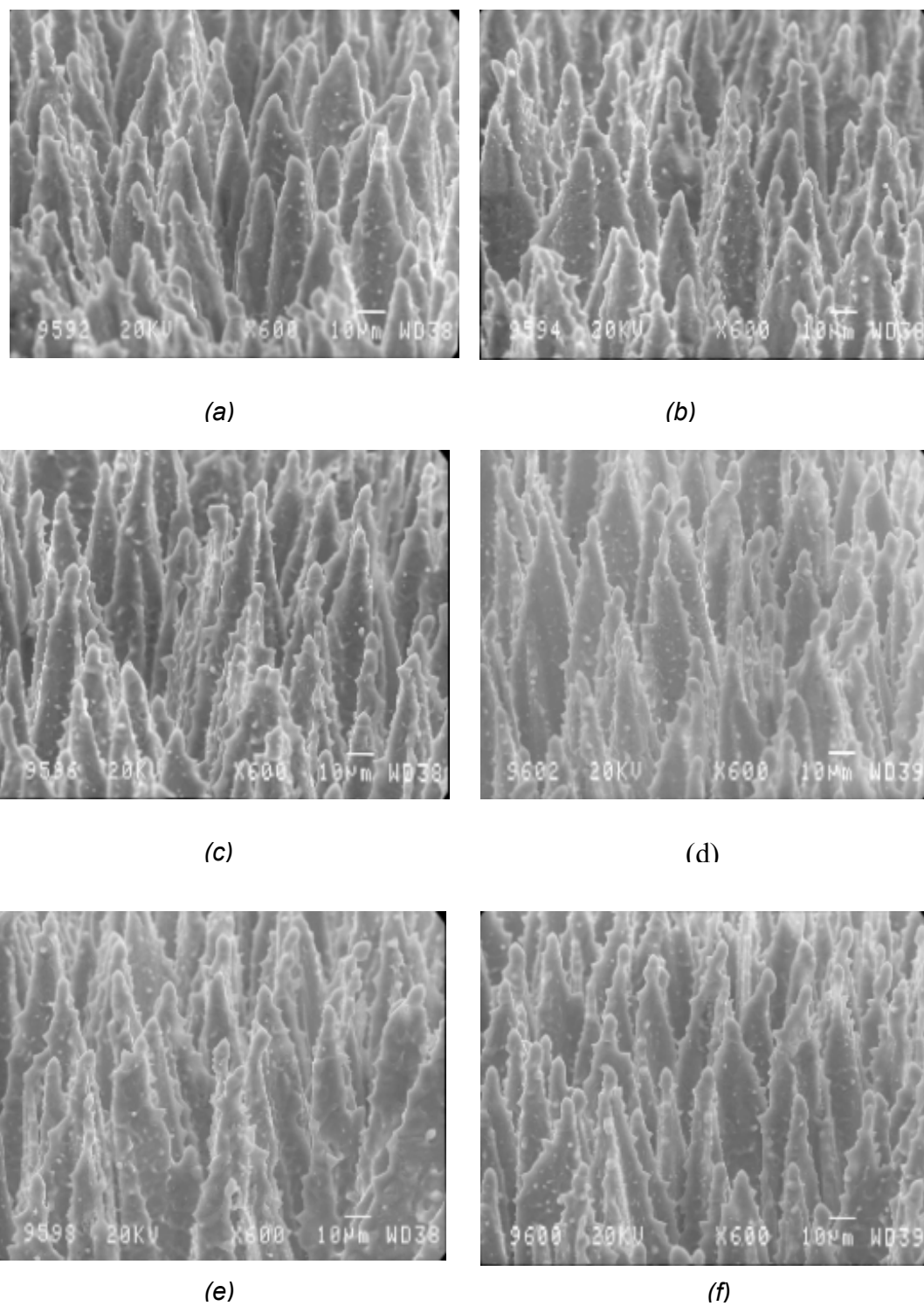
*(a)*



*(b)*



*(c)*



*(d)*



*(e)*



*(f)*
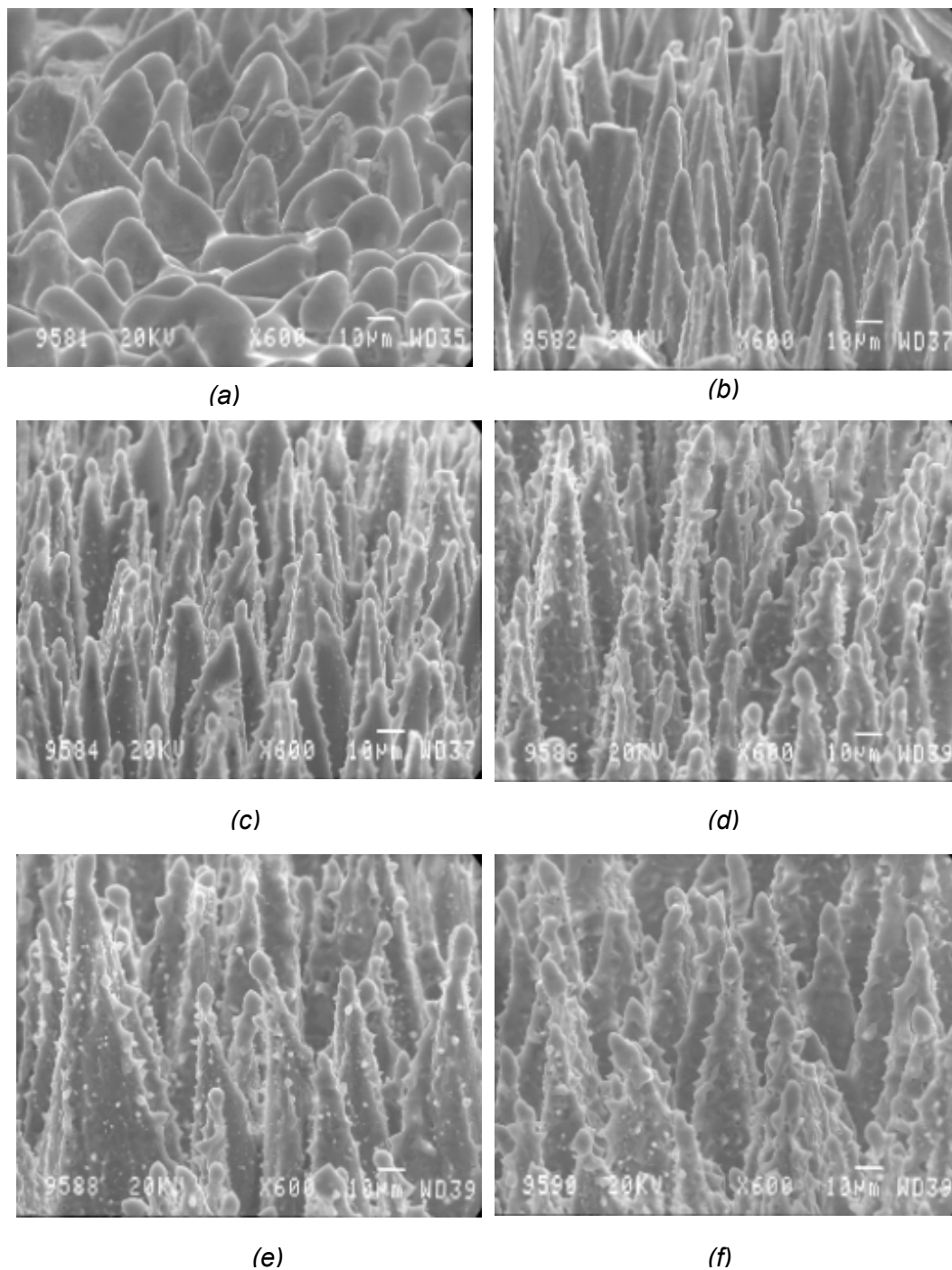
Fig. 5.6- SEM view (45°) of the ambient gas pressure influence on the obtained Si spikes morphology, upon irradiation with 1000pulses of a XeCl ($\lambda$=308nm, $\tau_{FWHM}$=32ns) excimer laser, when took place in  (a) vacuum, (b) 250 Torr $SF_6$ , (c) 500 Torr $SF_6$, (d) 750 Torr $SF_6$, (e) 1000 Torr $SF_6$ and (f) 1250 Torr $SF_6$ conditions. The laser fluence was set at 3,5J/$cm^2$. The laser repetition rate was 5 Hz

(a)                                           (b)

(c)                                           (d)

(e)                                           (f)

Fig. 5.7- SEM view (45°) of the laser repetition rate influence on the obtained Si spikes morphology, upon irradiation with 1000pulses of a XeCl ($\lambda$=308nm, $\tau_{FWHM}$=32ns) excimer laser delivering pulses at (a) 1 Hz, (b) 2 Hz, (c) 5 Hz, (d) 10Hz, (e) 15 Hz and (f) 20 Hz in the presence of 500 Torr $SF_6$. The laser fluence was set at 3,5J/$cm^2$

## 5.2.2 Experiments with the KrF sub-ps laser source

This section demonstrates a parametric study, examining the influence of:

- Laser fluence,

- Number of laser pulses (i.e. irradiation time) and

- Ambient gas pressure ($SF_6$)

on the morphology of the Si microcolumns obtained using the KrF sub-ps laser source. As in section 5.2.1 information concerning the height and spike density as a function of the number of pulses and the laser fluence respectively will be shown.

Under the best conditions the obtained spikes had a tip diameter in the sub-micron region while their height reached up to 10 μm.

### 5.2.2-1 Laser Fluence Dependence

Figure 5.8 depicts the SEM images corresponding to silicon spikes obtained with the use of the KrF sub-ps laser source in the presence of 500Torr $SF_6$. The formation of elongated structures on silicon was studied employing this laser source, operating at a repetition rate of 3Hz, for laser fluences ranging between 251-825 mJ/cm$^2$. As is shown in Figure 5.9, the Si spikes separation dinstance increases (thus spikes density decreases) with increasing laser fluence. The threshold for spikes formation using this laser source is relatively low (~100 mJ/cm$^2$ for 500Torr SF6).

*(a)*                                                                      *(b)*

*(c)*                                                                      *(d)*

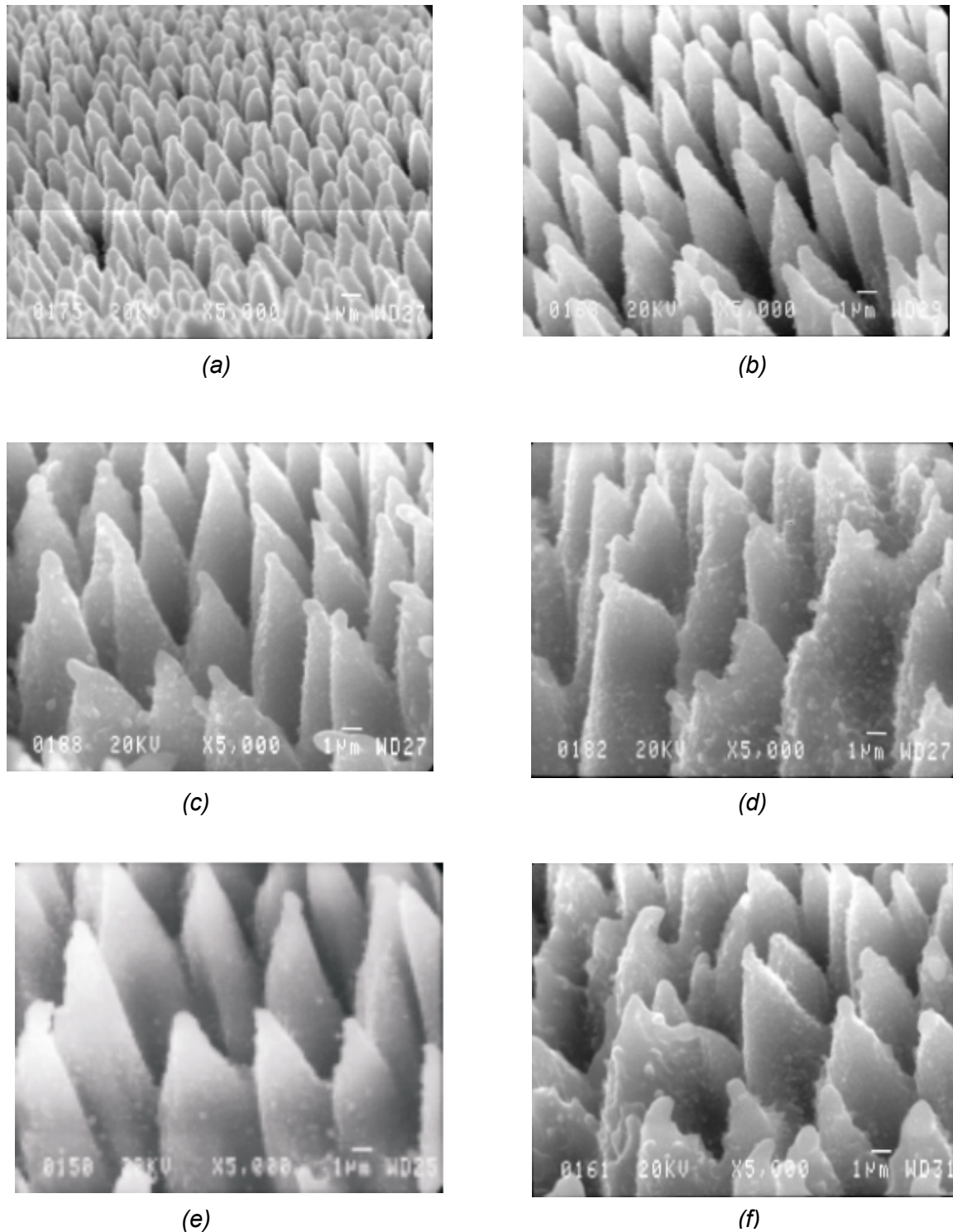*(e)*                                                                      *(f)*

Fig. 5.8- SEM view (45°) of the laser fluence influence on the obtained Si spikes morphology, upon irradiation with 1000pulses of a KrF ($\lambda$=248nm, $\tau_{FWHM}$=500 fs) excimer laser at a fluence of   (a)   251 mJ/cm$^2$, (b)   328 mJ/cm$^2$, (c) 504 mJ/cm$^2$, (d)  593 mJ/cm$^2$ (e) 628 mJ/cm$^2$ and (f) 825 mJ/cm$^2$. Microstructuring took place in the presence of 500 Torr SF$_6$. The laser repetition rate was 3Hz
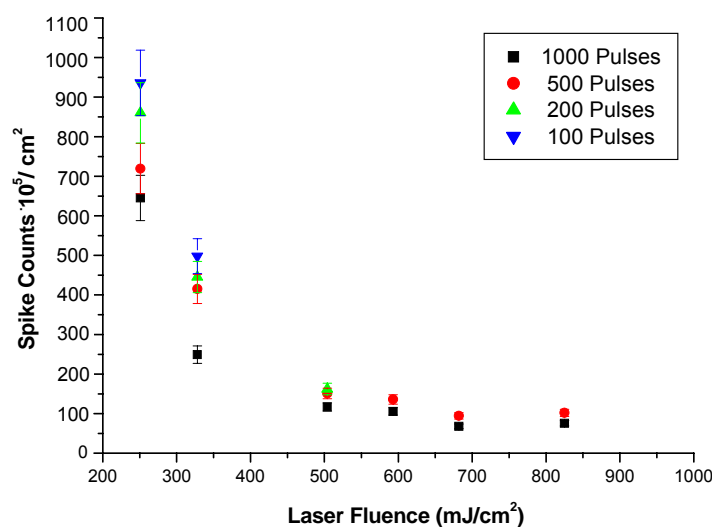
Figure 5.9-The average spike density (i.e. spike counts / area unit) as a function of laser fluence for varying number of pulses, using the KrF sub-ps laser source. Microstructuring took place in the presence of 500 Torr $SF_6$. The laser repetition rate was set at 3Hz.

## 5.2.2-2 Number of Pulses Dependence

SEM micrographs of the Si microcolumns obtained for varying number of pulses are shown in Figure 5.10. Increasing height of the obtained structures with increasing pulses (100-1000pulses) or increasing energy density [Figure 5.11]. A plateau beyond which the spikes do not grow further, was observed with this laser source. Microstructuring in this case took place in the presence of 500 Torr $SF_6$, while the laser repetition rate was set at 3 Hz.

(a)

(b)

(c)

(d)

(e)

(f)

(g)
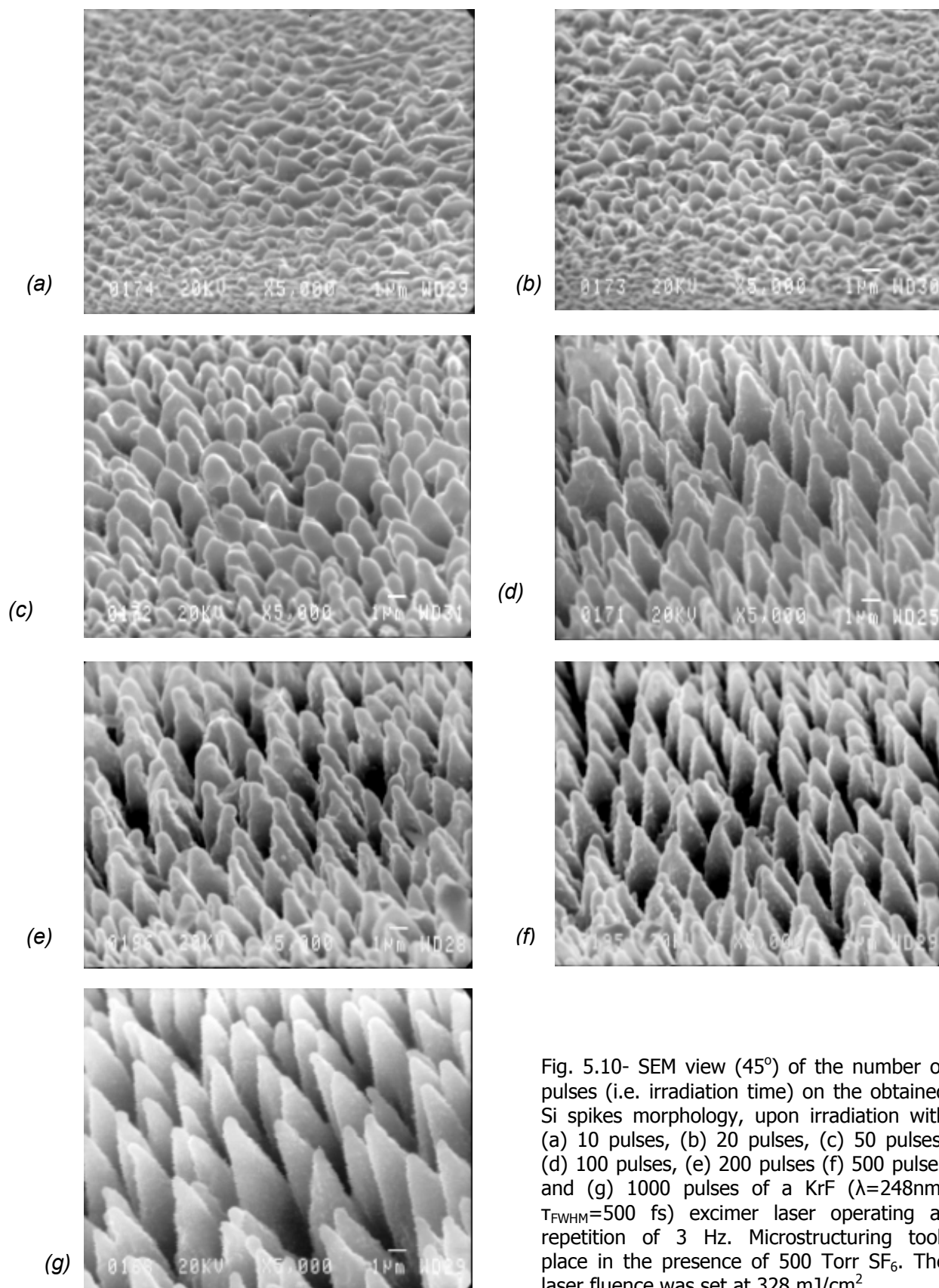
Fig. 5.10- SEM view (45°) of the number of pulses (i.e. irradiation time) on the obtained Si spikes morphology, upon irradiation with (a) 10 pulses, (b) 20 pulses, (c) 50 pulses, (d) 100 pulses, (e) 200 pulses (f) 500 pulses and (g) 1000 pulses of a KrF ($\lambda$=248nm, $\tau_{FWHM}$=500 fs) excimer laser operating at repetition of 3 Hz. Microstructuring took place in the presence of 500 Torr $SF_6$. The laser fluence was set at 328 mJ/cm$^2$
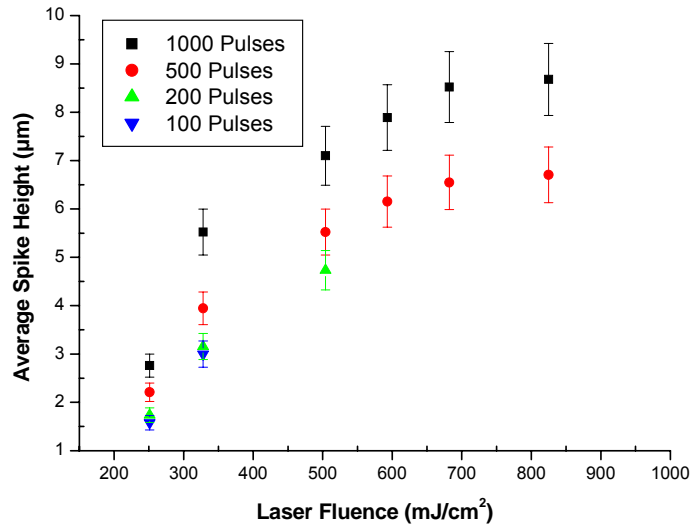
Figure 5.11-The variation of average spike height with increasing laser fluence for varying number of pulses, using the KrF sub-ps laser source. Microstructuring took place in the presence of 500 Torr $SF_6$. The laser repetition rate was set at 3Hz.

## 5.2.2-3 Ambient Gas Pressure Effect

Si spikes formation upon illumination with 1000 pulses of this sub-ps laser souce both in vacuum and with ranging $SF_6$ pressure was also studied. The irregular and blunt structures obtained in vacuum, become more pronounced with increasing ambient gas pressure (250-1250Torr $SF_6$) [Fig. 5.12]. A small number of secondary tips, a lot less pronounced than in the structures obtained with the XeCl* laser source, appear on the cone body for elevated values of $SF_6$ pressure (1000-1250 Torr). The laser fluence in this case was set at 328 mJ/cm$^2$, while the laser repetition rate was 3 Hz.
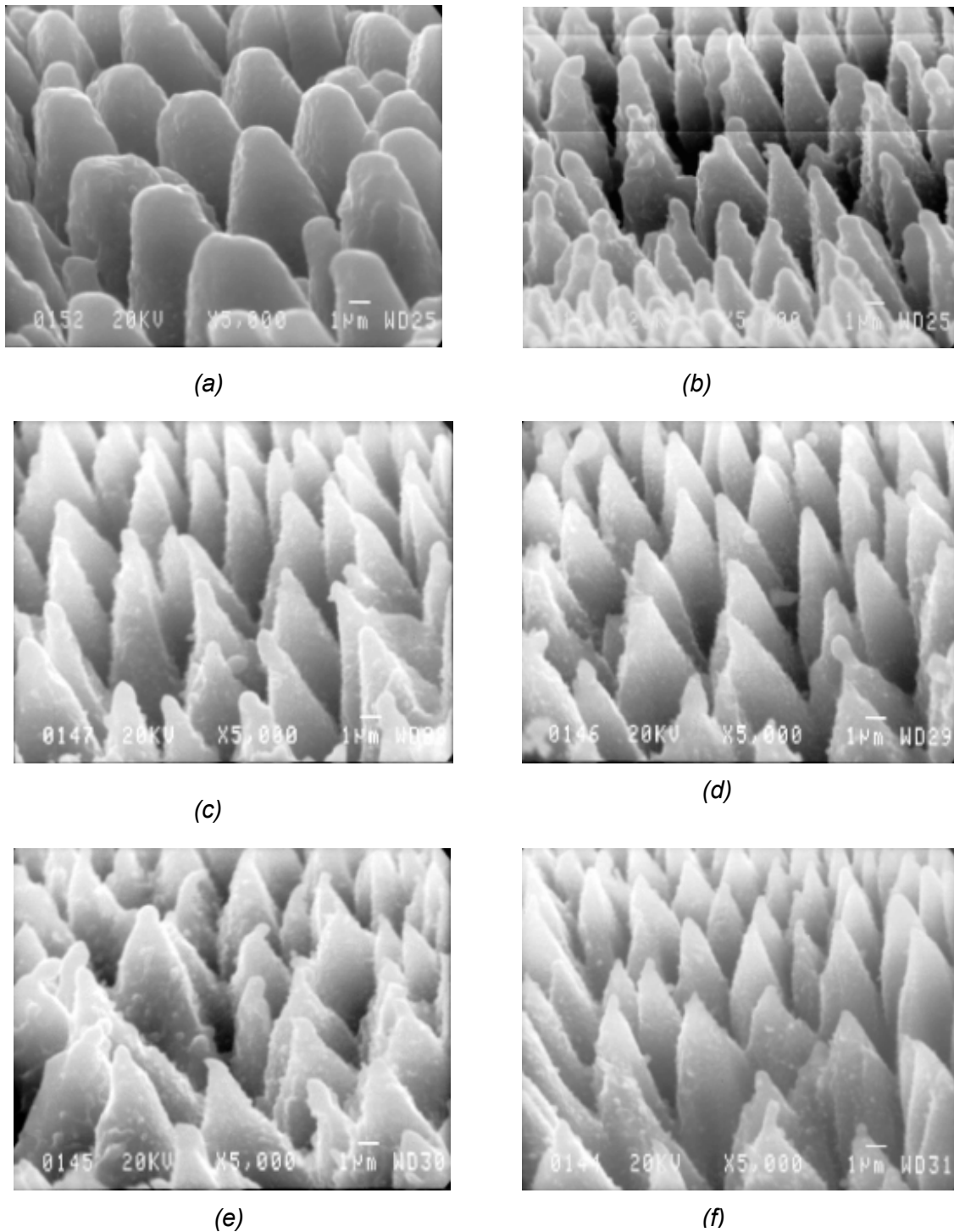
Fig. 5.12- SEM view (45°) of the ambient gas pressure influence on the obtained Si spikes morphology, upon irradiation with 1000pulses of a KrF ($\lambda$=248nm, $\tau_{FWHM}$=500 fs) excimer laser, when microstructuring took place in  (a) vacuum, (b) 250 Torr $SF_6$ , (c) 500 Torr $SF_6$, (d) 750 Torr $SF_6$, (e) 1000 Torr $SF_6$ and (f) 1250 Torr $SF_6$ conditions. The laser fluence was set at 328 mJ/cm$^2$. The laser repetition rate was 3 Hz

### 5.2.3 Experiments with the Ti:Sapphire fs laser source

This section demonstrates a parametric study, examining the effect of

- Laser fluence,

- Number of laser pulses (i.e. irradiation time)

- Ambient gas pressure ($SF_6$) and

- HF solution

on the size, distribution, and density of the conical features obtained, using the Ti:Sapphire laser source ($\lambda$=800 nm, $\tau_{FWHM}$=50 fs). Additional information concerning the height and spike density as a function of the number of pulses and the laser fluence respectively will be exhibited.

Under the best conditions the tip diameter of the obtained structures was as low as 500 nm, while their height reached up to 40μm.

### 5.2.3-2 Laser Fluence Dependence

Spikes evolution was studied upon illumination with 1000 pulses at a repetition rate of 1 kHz with laser fluence ranging from 0,16 to 1.16 J/cm$^2$  [Fig 5.13]. Microstructuring took place in the presence of 500 Torr $SF_6$. Under these conditions, no spikes were formed for fluences lower than 0,32 J/cm$^2$.
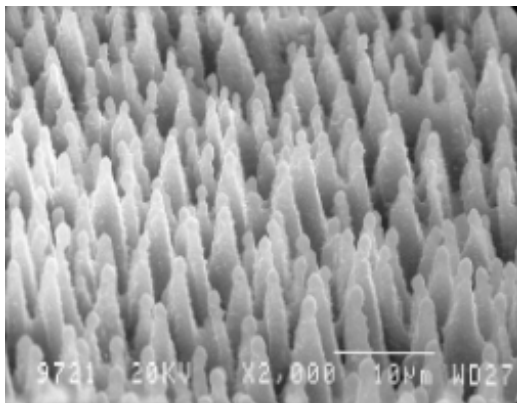
As has also been observed with the other two laser sources, the spikes separation distance increases (thus spikes density decreases) with increasing laser fluence [Fig. 5.14].
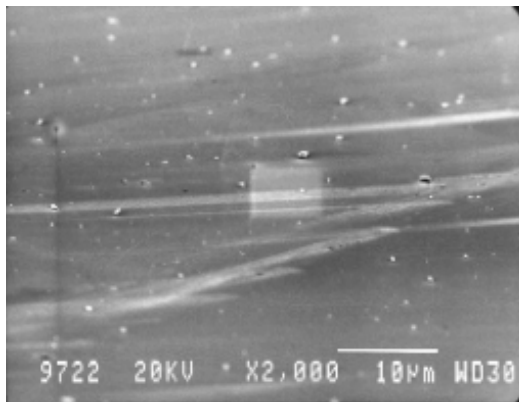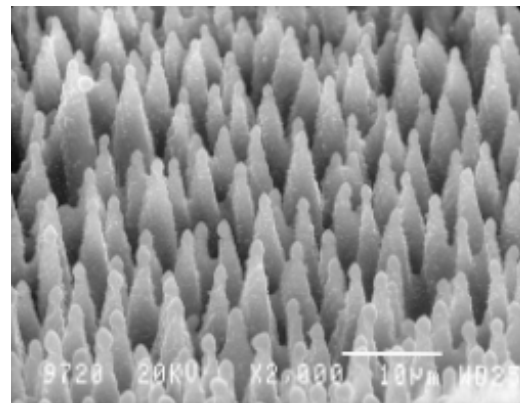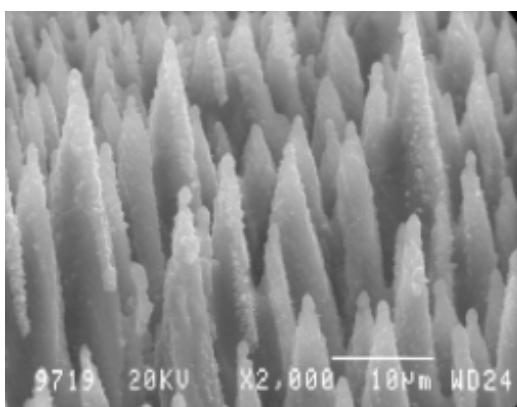
*(a)*
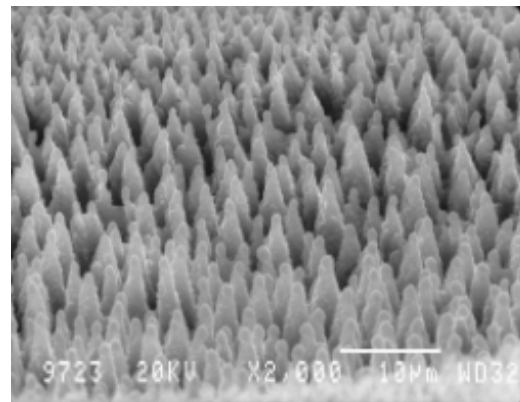


*(b)*



*(c)*



*(d)*



*(e)*

Fig. 5.13- SEM view (45°) of the laser fluence influence on the obtained Si spikes morphology, upon irradiation with 1000pulses of a Ti:Sapphire ($\lambda$=800nm, $\tau_{FWHM}$=50fs) laser at a fluence of (a) 0,16 J/cm$^2$, (b) 0,32 J/cm$^2$, (c) 0,58 J/cm$^2$, (d) 0,84 J/cm$^2$ and (e) 1,16 J/cm$^2$. Microstructuring took place in the presence of 500 Torr SF$_6$. The laser repetition rate was 1kHz
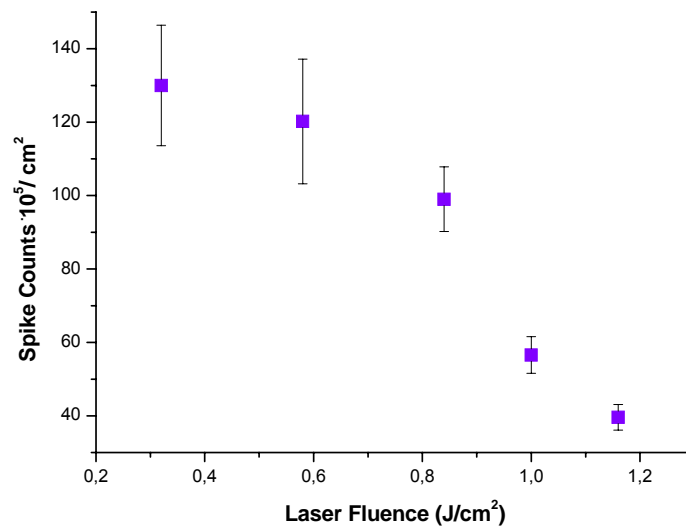
Figure 5.14- Spikes Density (i.e. spike counts / area unit) as a function of laser fluence, for Si spikes obtained using the Ti:Sapphire (fs) laser source

### 5.2.3-2 Number of Pulses Dependence

Figure 5.16 shows a set of SEM micrographs of Si micro-columns obtained with the employment of the Ti:Sapphire fs laser source. An increase in the average spike height was observed with increasing laser pulses, for number of pulses ranging from 250 to 3000 [Fig. 5.16]. Microstructuring in this case took place in the presence of 500 Torr $SF_6$. The laser fluence was set at 1,16 $J/cm^2$ while the laser repetition rate was 1 kHz. With this laser source also, the existence of a plateau in number of pulses beyond which no further growth is seen, is observed [Fig. 5.15].
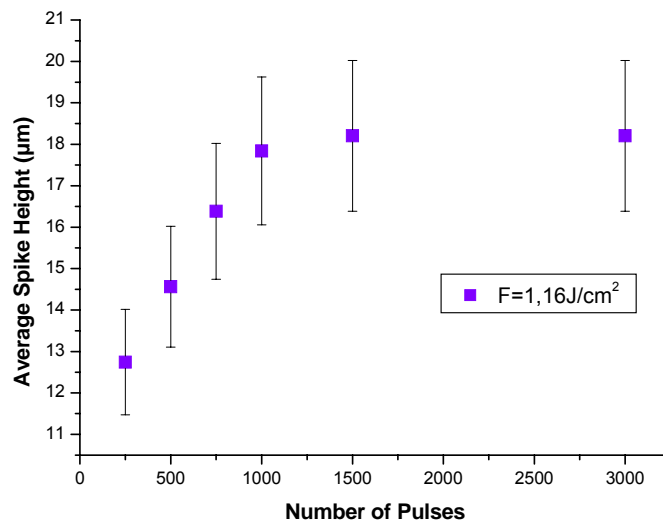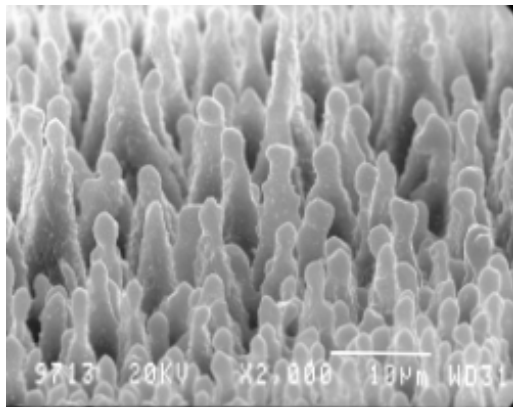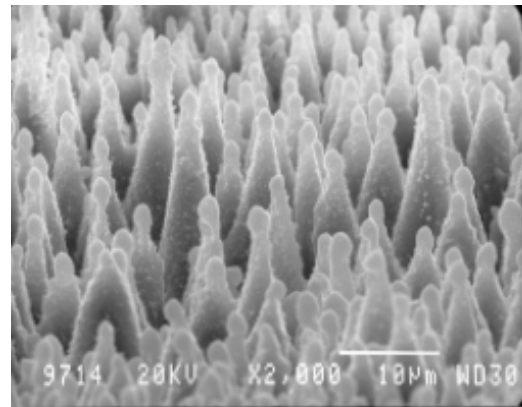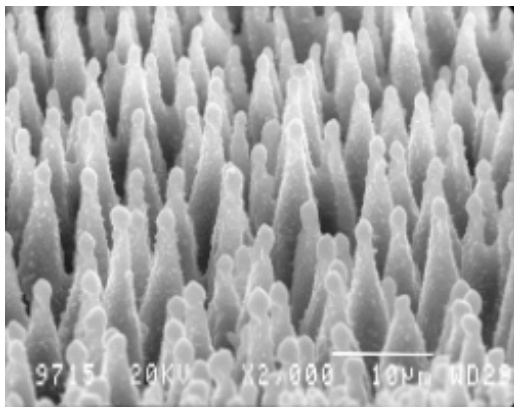
Figure 5.15- Spikes Average Height (in μm) as a function of the Number of Pulses, for Si spikes obtained using the Ti:Sapphire (fs) laser source

(a)



(b)



(c)



(d)
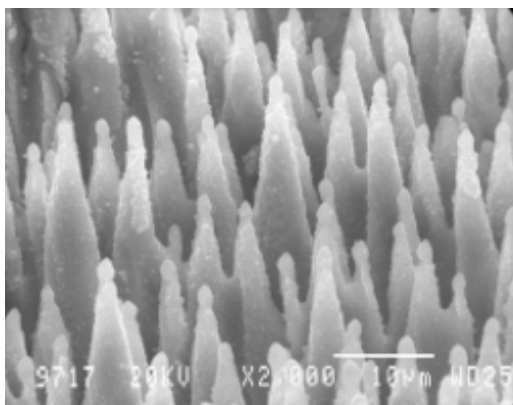


(e)
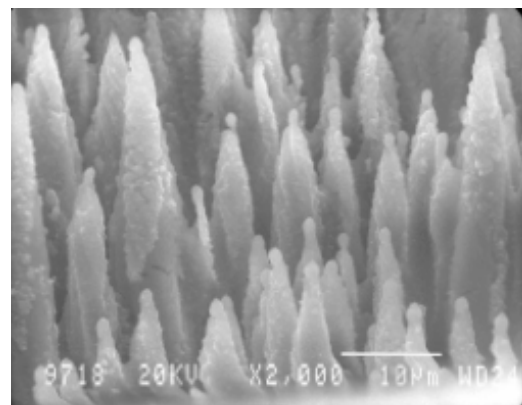


(f)

Fig. 516- SEM view (45°) of the number of pulses (i.e. irradiation time) on the obtained Si spikes morphology, upon irradiation with a Ti:Sapphire (λ=800nm, τ$_{FWHM}$=50fs) laser in the case when (a) 250 pulses, (b) 500 pulses, (c) 750 pulses, (d) 1000 pulses, (e) 1500 pulses and (f) 3000 pulses (g) 3000 pulses were used. Microstructuring took place  in the presence of 500 Torr SF$_6$. The laser fluence was set at 1,16 J/cm$^2$ while the laser repetition rate was 1 kHz.

### 5.2.3-3 Ambient Gas Pressure Effect

The formation of Si spikes both in vacuum and with ranging ambient gas pressure ($SF_6$) was studied [Fig. 5.17] using the above mentioned laser source, delivering pulses at a repetition rate of 1kHz. The laser fluence was set at 0,58 J/cm$^2$

The Si structures obtained in vacuum were blunt and irregular. However they became more pronounced with increasing ambient gas pressure (250-1250Torr). In agreement to Her et al. [51] the presence of a spherical cap on the top of these structures was observed in relatively low gas pressure (i.e. ~500Torr or less). The spherical shape of the caps suggests that they are due to resolidification of a liquid silicon drop before the liquid can wet the sharp spike [4]. However this effect it is a lot less pronounced for elevated pressures (i.e. 1000-1250 Torr). Moreover the threshold fluence for spikes formation is reduced with increasing $SF_6$ pressure
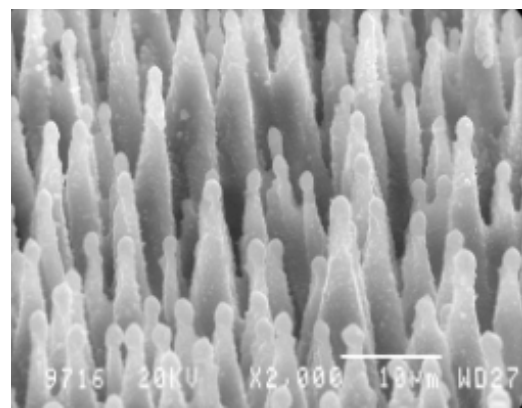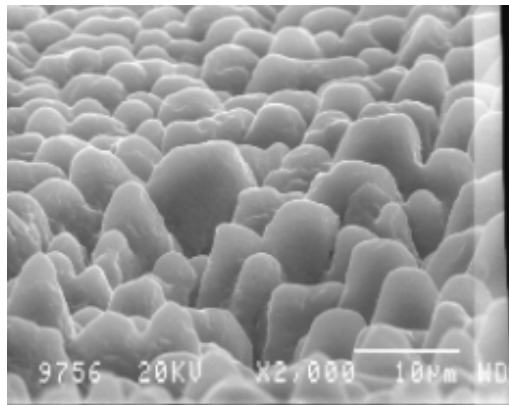
(a)
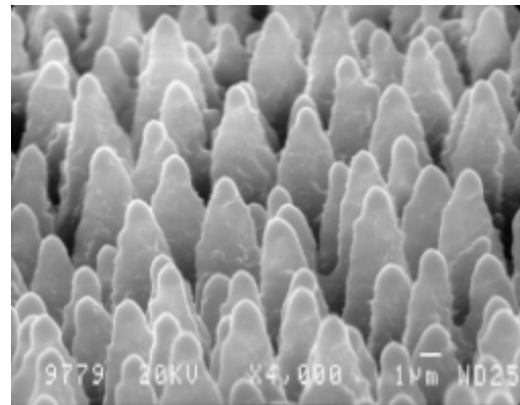


(b)
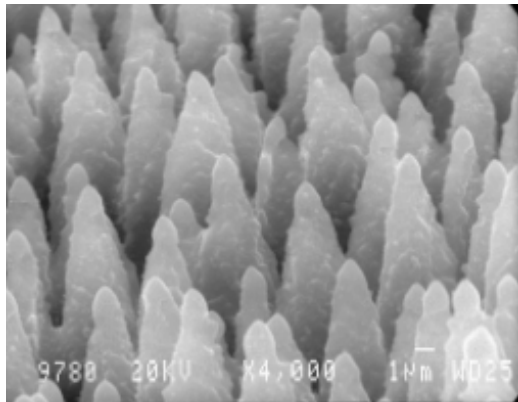


(c)
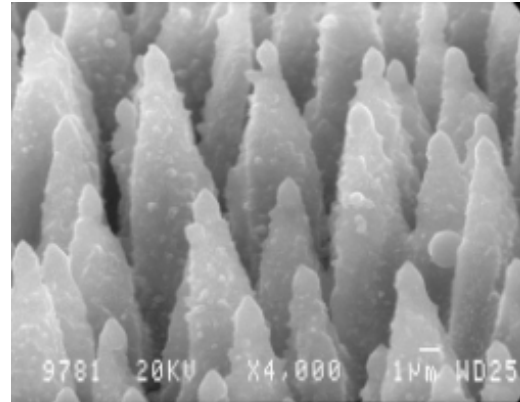


(d)
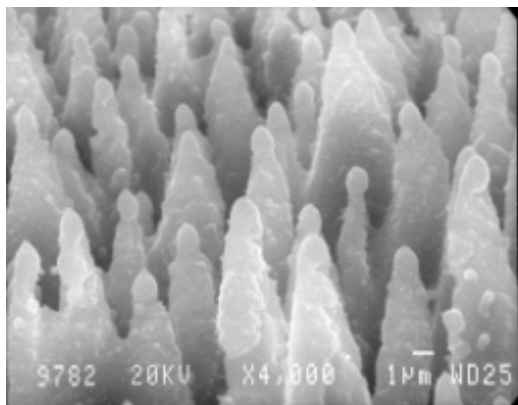


(e)
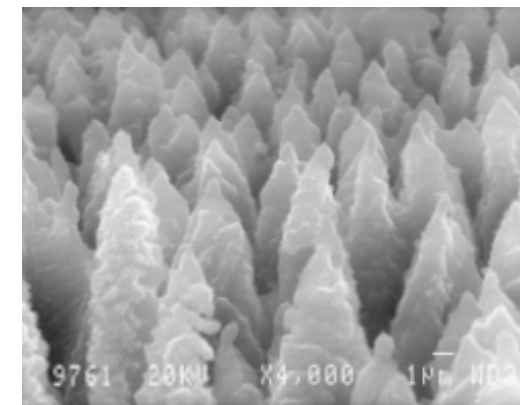


(f)

Fig. 5.17- SEM view (45°) of the ambient gas pressure influence on the obtained Si spikes morphology, upon irradiation with 1000pulses of a Ti:Sapphire ($\lambda$=800nm, $\tau_{FWHM}$=50fs) laser, when microstructuring took place in (a) vacuum, (b) 250 Torr $SF_6$ , (c) 500 Torr $SF_6$, (d) 750 Torr $SF_6$, (e) 1000 Torr $SF_6$ and (f) 1250 Torr $SF_6$ conditions. The laser fluence was set at 0,58 J/cm$^2$. The laser repetition rate was 1 kHz

### 5.2.3-4 HF Effect

The effect of HF as an etching agent for silicon oxide remnants was also studied [Fig. 5.18] by rinsing the samples in an aqueous solution of 10 % HF. No evident change in the spherical cap dimensions or morphology was observed, however there was an obvious reduction in the cone body diameter, of the order of a few hundredth nanometers.



*(a)*



*(b)*



*(c)*



*(d)*
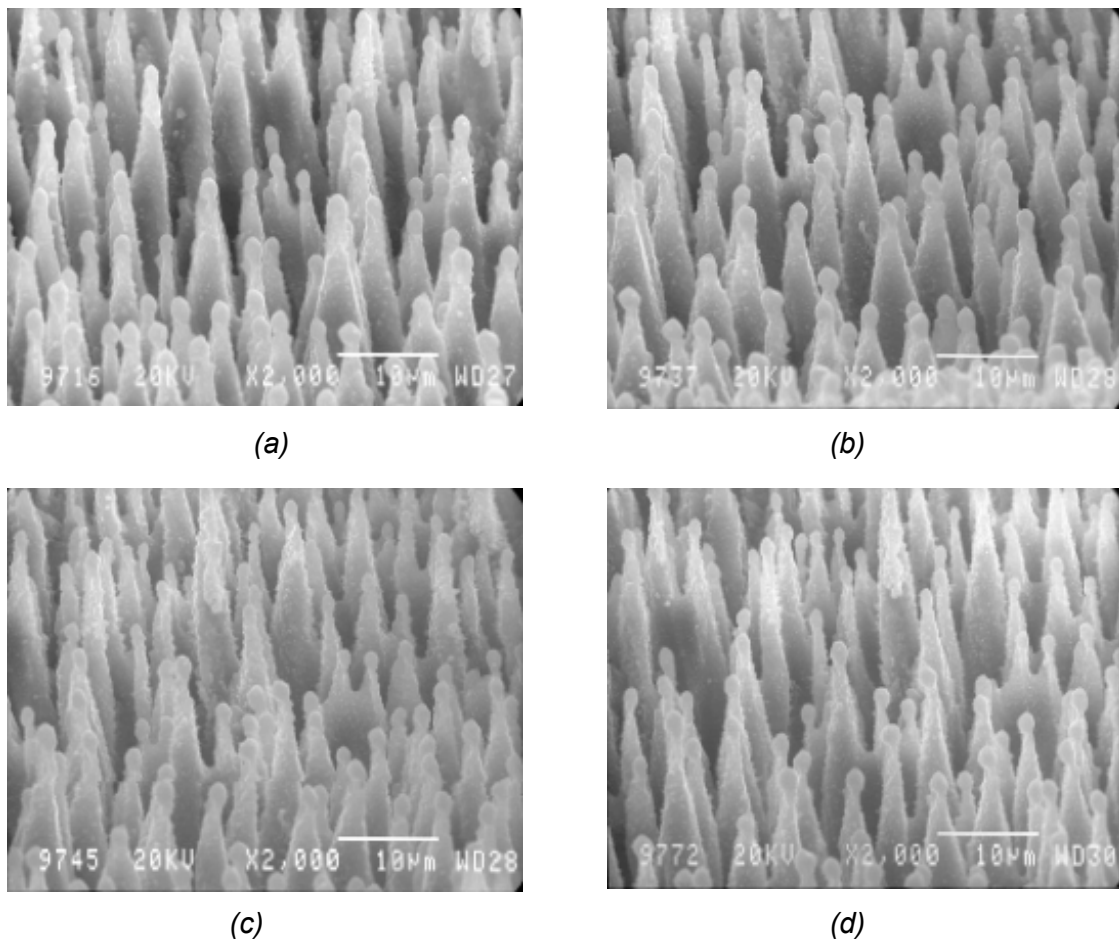
Fig. 5.18- SEM view (45°) of the HF influence on the obtained Si spikes morphology when (a) No HF was used or after a (b) 5min, (c) 15 min and (d) 1h and 45min bath in a 10% HF aqueous solution. 1000pulses of Ti:Sapphire ($\lambda$=800nm, $\tau_{FWHM}$=50fs) laser source were used at a fluence of 1.1 J/cm$^2$ Microstructuring took place in the presence of 500 Torr SF$_6$ while the laser repetition rate was 1 kHz

Experiments were also carried out by illuminating samples in intervals employing a constant number of pulses (e.g. 200 x 5 or 100 x 10) and variable delays (0.1-2 sec). However it appeared to have no evident effect on the quality of the microstructures obtained.

### 5.2.4 General Remarks

As a few common trends in the obtained Si spikes morphology were observed, independently on the laser source (ns, sub-ps or fs) employed. :

- The density of the obtained spikes decreases with increasing laser fluence. This observation is consistent with the capillary-wave driven formation. Increasing the fluence deposits more energy in the Si substrate, melting more Si and therefore increasing the liquid layer depth and lifetime [52]. On this basis, as may be derived from the dispersion relation for capillary waves, increasing the laser fluence should correspond to the formation of capillary waves with higher spatial period.

  Moreover, the density of the spikes in the centre of the spot is much smaller than in outer parts. This implies that melting in the central part of the spot is increased as compared to the outer parts (as should be expected assuming a gaussian energy distribution of the beam), leading to increased melting, and thus a longer wavelength of the capillary waves at the given region.

- It has been observed that the spikes height increases with increasing number of pulses (i.e. irradiation time), until approaching a plateau beyond which no growth is further observed. Growth of spikes as discussed in Chapter 3, is mainly attributed to preferential material removal in the intercone areas due to a variation of the reflectivity of the rough surface. In this context, a plausible explanation for this plateau observation is that the increasing height of cones leads to a reduction of the angle formed in between cones and thus reducing the free surface at normal incidence to the laser beam.

- The Si spikes formed in vacuum are blunt and irregular. However they become more pronounced with increasing $SF_6$ pressure. Increase of secondary tip decoration (of the order of a few tens or hundredth nanometers) on the cone tip

bodies at elevated $SF_6$ pressures (i.e. 1000-1250 Torr) is also observed. This could be interpreted in terms of an increased interaction cross section of $SF_6$ molecules with the Si surface due to the increased reactive gas concentration.

## 5.3 MECHANISTIC ASPECTS

### 5.3.1 The Laser Pulse Duration Effect

Figure 5.19 depicts a cross sectional view of the Si spikes obtained using the Ti:Sapphire (fs) and the XeCl (ns) laser source respectively. A striking feature is the fact that the structures formed with the XeCl laser source protruded tens of microns above the initial surface in oppose to the Ti: Sapphire laser source where the spikes do not protrude above the initial surface at all. The same trend was observed in the case when microstructuring took place using the KrF (sub-ps) laser source.



100μm
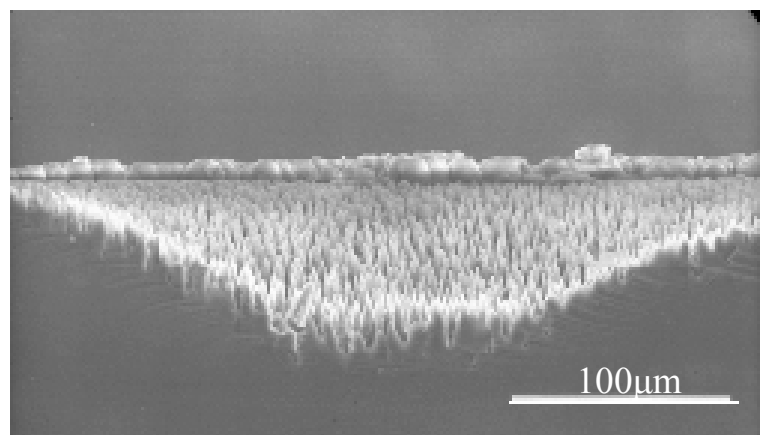
(a)
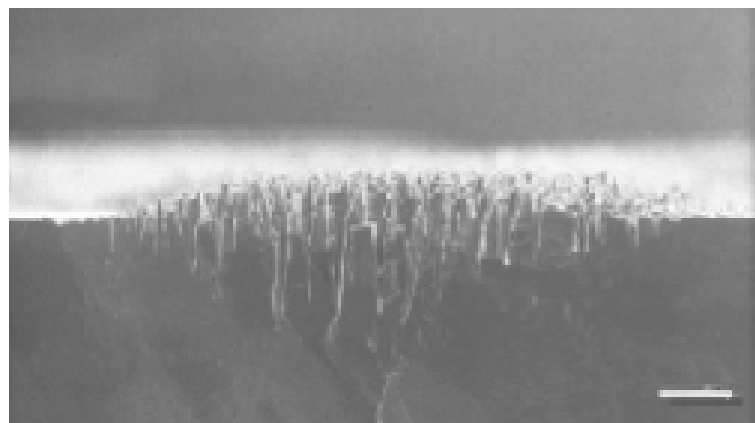


(b)

Figure 5.19- Cross sectional view of Si spikes obtained in an SF6 atmosphere using (a) the Ti:Sapphire laser source and (b) the XeCl excimer laser source

As has been extensively discussed in Chapter 3, Si spikes grow from the initial fluctuations (capillary waves) towards the laser beam axis, so their spatial period is determined by the melt parameter. The formation of elongated cone-like structures is attributed to preferential material removal of material at certain locations, owing to the increase of reflectivity of the surface with the increase of the incident angle. This causes material to be removed mostly in those areas of the wafer that are oriented to the normal of the laser beam,  that is between the cones.

### 5.3.1-1 Si Microstructuring Utilizing ns laser pulses

In the case that ns laser pulses are employed for Si microstructuring, growth should involve redeposition (not merely erosion) since the obtained cones grow well above the surrounding surface. It has been suggested that growth occurs by a "catalyst free" VLS (vapor-liquid-solid) mechanism [53] that involves repetitive melting of the tips of the columns/cones and redeposition there of the ablated flux of Si-containing vapor produced by ablation of the surface region between columns (especially from pits or grooves). This mechanism explains the fact that Si spikes protrude above the initial surface.

### 5.3.1-2 Si Microstructuring Utilizing fs laser pulses

The fact that the structures made with fs pulses have not been seen to protrude above the initial Si surface suggests that ablation or removal of Si by chemical etching in this case is dominant over redeposition. The presence of nearly spherical tips of cones made by fs irradiation has been explained as the result of resolidification of a molten droplet. This phenomenon has been observed in the past however when ns irradiation was applied [54]. The presence of this resolidified molten droplets at the tips of the obtained Si cones opens up the possibility that a VLS growth mechanism similar to that observed for ns irradiation operates with fs pulses as well.

The structures made with different pulse durations exhibit many qualitative similarities so we can assume that a similar process is operative for their formation. However it is clear that that the balance between these processes is different in each case.

### *5.3.2 Estimation of Capillary Waves Spatial Period*

A qualitative approximation of the nature of the laser interaction with Si surfaces, considering the different laser sources used, may be obtained by estimating the optical penetration depth ($L_{opt}$) and the thermal diffusion length ($L_{th}$) in the Si bulk in each case. Employing Equations [3.3] and [3.4] respectively, we obtain the following values [Table 5.1].

| | KrF (248nm,500fs) | XeCl (308nm,32ns) | Ti:Sap (800nm, 50fs) |
|---|---|---|---|
| Optical Penetration Depth | 11,077nm | 13,673nm | 25,478µm |
| *Thermal Diffusion Length* | 9,49nm | 2,4µm | 3nm |

Table 5.1- *Calculated values for $L_{opt}$ and $L_{th}$ for each of the three different laser sources employed*

For the calculations exhibited at Table 5.1 the data shown in Table 5.2 were used:

| Si - Single Crystal | | | | |
|---|---|---|---|---|
| **Thermodynamic Properties** | | **Optical Properties** | | |
| | | λ | κ | R (φ=0) |
| P | 42,33 gr/cm$^3$ | 248nm | 3.565 | 0,675 |
| $C_v$ | 0,71 J/gK | 308nm | 3,587 | 0,591 |
| K | 149 J/ m·sec·deg | 800nm | 5 x 10$^{-3}$ | 0,327 |

Table 5.2- *Thermodynamic and optical properties of single crystalline Si*

As has been discussed in Chapter 3, the wavelength of the capillary waves formed on Si during laser irradiation is given by

$$\lambda_c = \left[\frac{\alpha \cdot h}{\rho}\right]^{1/4} \cdot \left(2 \cdot \pi \cdot \tau_c\right)^{1/2}$$

*(Eq. 5.1)*

where a is the surface-tension coefficient of the air/liquid interface, $\rho$ is the density of the liquid, h is the thickness of the liquid, $\tau_c$ is the period of the capillary wave and $\lambda_c$ is the wavelength of the capillary wave.

The capillary wave period cannot exceed the lifetime of the liquid layer $\tau_{liq}$, and therefore the average spike separation cannot exceed the wavelength corresponding to wavelength corresponding to $\tau_{liq}$. Through a simple model [52] (that ignores the effect of ablation) we can estimate the time of existence of the liquid layer using Equation 5.2

$$\tau_{liq} \sim \frac{L^2}{2 \cdot D_{th}}$$

*(Eq. 5.2)*

Setting L and h as the highest value of $L_{opt}$ or $L_{th}$ for the case of each laser source, in combination with the data given on Tables 5.1 and 5.2, an approximate analysis of the capillary waves wavelength may be extracted (Table 5.3).

| Laser Source | $\lambda_c$ *(Calculated Value )* | $\lambda_c$ *(Experimental Value )* |
|:---:|:---:|:---:|
| KrF | 9.1 nm | ~3μm |
| XeCl | 2.4 μm | ~15-20μm |
| Ti:Sap | 46.8 μm | ~5-10 μm |

Table 5.3- Calculated values of the capillary waves wavelength corresponding to each laser source, and comparison to the wavelength of the capillary waves as measured on the microstructured Si samples.

As is shown in Table 5.3, these calculated values are not consistent with the spatial period of the capillary waves observed in the microstructured samples. This is probably due to the fact that phenomena related to fundamental interactions are not taken into account in these estimations.

For instance as is shown in Eq.5.2 the liquid depth is nowhere correlated to the intensity of the laser pulse. However the liquid depth and consequently, the spatial period of the capillary waves formed on the Si surface are strongly dependent on the laser fluence. In this respect, the estimation of the capillary waves wavelength is rather rough, and is not representative of the processes taking place during laser interaction with Si, under the given conditions.

In any case for the data obtained for interactions with fs lasers there is a serious source of uncertainty in the optical penetration depth, which may be strongly influenced due to the presence of non-linear effects (e.g. multi-photon processes). Also the extrapolation of heat diffusion models developed for ns or longer pulse durations is questionable and may be an additional source of the deviations observed at these ultrashort pulse duration scales.

### 5.3.3 The role of the reactive gas (SF$_6$)

As has already been underlined, the Si spikes formed in vacuum are blunt and irregular, while they become more pronounced with increasing SF$_6$ pressure. Similar behaviour has been observed in halogen containing atmospheres (e.g. Cl$_2$ [55]). Also of interest is the observation that Si spikes do not form in a neutral atmosphere such as Ar [56] or N$_2$. This enhances the assumption that Si spikes formation is a synergy of laser matter interaction and laser assisted chemical etching.

When resonant excitation is considered multiphoton absorption of SF$_6$ molecules is expected to place for intensities exceeding $10^6$ W/cm$^2$. The high intensities obtained with the laser sources employed for this set of experiments (I=$10^8$ W/cm$^2$, I=2 $10^{10}$ W/cm$^2$, I=2 $10^{13}$ W/cm$^2$ for the ns, the sub-ps and the fs laser source respectively) suggest that multiphoton phenomena are bound to take place.

| State | $T_o$ | Vibrational Frequencies | | | | | | Observed Transitions |
|---|---|---|---|---|---|---|---|---|
| | | v1 | v2 | v3 | v4 | v4 | v6 | |
| $\widetilde{F}$ | (118250) | Continuous absorption | | | | | | $\widetilde{X} \to \widetilde{F}$   846-815 Å |
| $\widetilde{E}$ | (112000) | << | | | | | | $\widetilde{X} \to \widetilde{E}$   893-852 Å |
| $\widetilde{D}$ | (106000) | << | | | | | | $\widetilde{X} \to \widetilde{D}$   944-929 Å |
| $\widetilde{C}$ | (90400) | << | | | | | | $\widetilde{X} \to \widetilde{C}$   1120-1000 Å |
| $\widetilde{B}$ | (63980) | << | | | | | | $\widetilde{X} \to \widetilde{B}$ (v)  1563 Å- |
| $\widetilde{A}$ | (46000) | << | | | | | | $\widetilde{X} \to \widetilde{A}$ (v)  2170 Å- |
| $\widetilde{X}\ ^1A_{1g}$ | 0 | 769.4 | 639.5 | 940 | 614 | 522 | 344 | Infrared and Raman Spectra |

Table 6.4- Molecular constants in the electronic states of $SF_6$.   [57]

Considering 3hv or 4hv resonant excitation for the employed wavelengths, the following transitions may occur:

- 248nm: 3photon absorption = 826 Å  corresponding to X→F transition
- 308nm:        >>            =1027 Å corresponding to X→C transition
- 800nm:  4     >>            = 2000 Å corresponding to X→A-B transition

All these transitions lead to dissociative states of $SF_6$ and therefore $SF_x$ and F radicals may be produced. The etching role of $SF_6$ is attributed to the presence of these radicals.

A possible scenario [58] explaining how $SF_6$ may react with the Si surface is the following  (Fig. 5.20):

- Laser pulses are focused onto the Si surface.
- The high intensity pulses (due to focusing) disrupt the molecules close to the surface leading to the creation of reactive fluorine radicals [Fig. 5.20(b)].
- These radicals react with silicon (possibly in a liquid form) and form $SiF_x$ compounds [Fig. 5.20(c)].
- These compounds are desorbed by the laser, while volatile species (such as $SiF_4$) leave the surface [Fig. 5.20(d)].
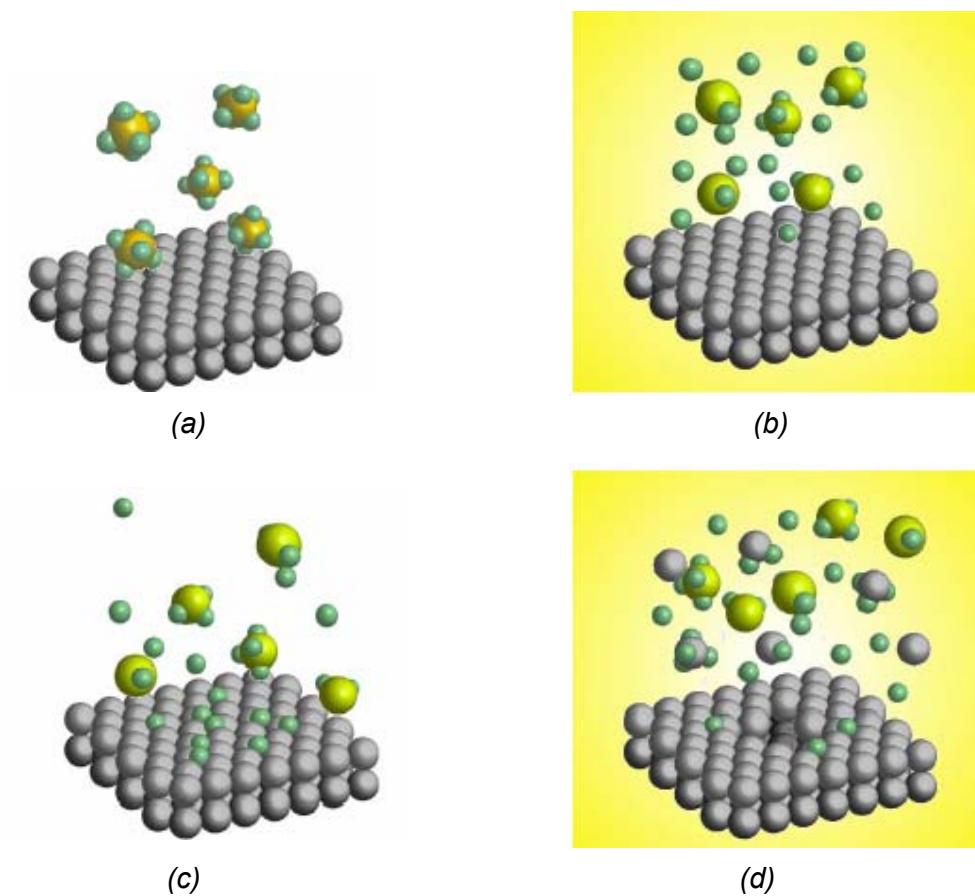
*(a)*

*(b)*

*(c)*

*(d)*

Fig. 5.20- Possible interaction mechanism of SF$_6$ with Si

---

[v] Not certain that $\widetilde{A}$ and $\widetilde{B}$ are different

## 5.4 FIELD EMISSION PROPERTIES

### *5.4.1 Field Emission Testing*

Field emission testing requires areas minimum of 0.04 cm$^2$ so large area microstructuring was required. Figure 5.21 depicts a typical example of the morphology over large areas.
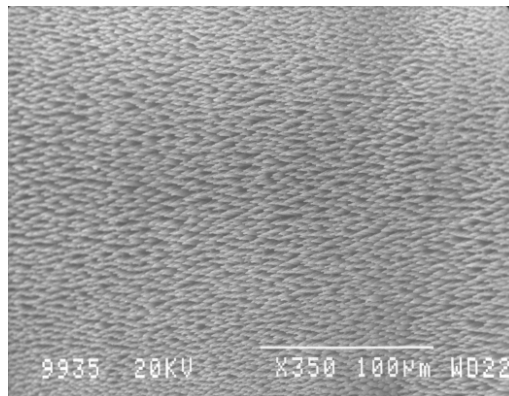


Fig. 5.21 - Typical SEM photo of spikes formed over a large area using the Ti:Sapphire laser source operating at 1kHz. The fluence was 0.55 J/cm$^2$ while 100 pulses/step were applied. The overlap between consecutive scans of the laser beam was 80%.

The current-voltage (I-V) field emission characteristics of a 2x2 mm$^2$ area of micro-structured n-type Si using the Ti:Sapphire laser beam is shown in Fig. 5.20. The laser fluence was 1 J/cm$^2$ , the overlap between consecutive scans was 75%, while the Si surface was irradiated with 88 pulses/step.

After conditioning, the field emission threshold for the studied Si tips. The Fowler-Nordheim Field emission is studied by progressively increasing the maximum applied field similar to a conditioning cycle, and recording the emission current during increasing and decreasing the applied electric field. The filled triangles in Fig. 5.22 show the I-V curve when the maximum electric field of 6.4 V/μm is applied. The emission current increases suddenly by 100 times when the applied field is increased up to 6.8 V/μm (open diamonds). Surface irregularities may result in micro-arcing but the sudden increase in current lasts only for a few data points. On the contrary, in our case I-V measurement after half hour (crosses) follows the improved field emission characteristics. After several conditioning

cycles, the field emission threshold for the studied Si tips is as low as 2 V/μm, with an emission current of $10^{-3}$ A/cm$^2$ at 4 V/μm.

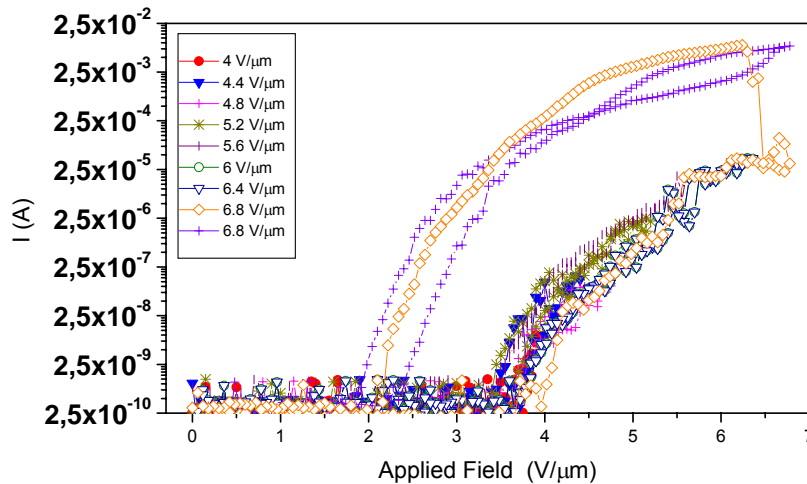

Figure 5.22- Field emission I-V characteristics of a 0,04 cm$^2$ Si area microstructured using a Ti:Sapphire laser beam in 500 Torr SF$_6$ pressure. The externally applied electric field was increased in successive cycles and the emission current was measured during increase and decrease of applied voltage

An interesting feature, is that the field emission threshold these structures exhibit, is comparable to that of good quality carbon nanotubes, despite the fact that their aspect ratio is a lot smaller.

### 5.4.2 Field Enhancement Factor Calculations

According to the Fowler-Nordheim plot (Eq.2.9), there is an exponential relation correlating the current density output attributed to field emission to the applied field. If we plot $\log(J/\varepsilon^2)$ vs. $1/\varepsilon$ and get a straight line it is reasonable to deduce that the current density comes from field emitted electrons. Fitting the experimental data with a function of the form of $J/\varepsilon^2 = A\exp[B/\varepsilon]$ allows one to determine the quantities A, B. When the applied field is amplified, then quantity B becomes $-6.8 \times 10^{11} \Phi^{3/2}/\beta$, $\beta$ being the amplification factor.

Figure 6.3 shows the Fowler-Nordheim plot of the I-V measurements, as illustrated in Figure 5.20.
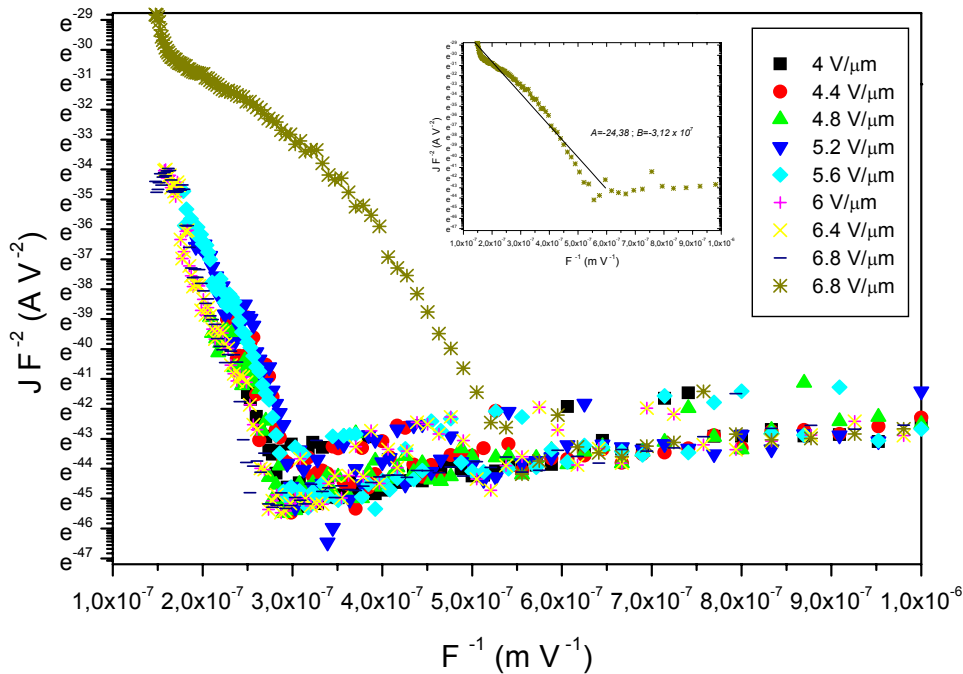


Figure 5.23-The Fowler-Nordheim plot of the I-V data of a 0,04 cm$^2$ Si area microstructured using a Ti:Sapphire laser beam in 500 Torr SF$_6$ pressure.

The inset of Figure 5.23 shows the fit of the experimental data for the curve corresponding to the lowest field emission threshold. The fit in this case is a straight line. Its slope, as extracted through the linear fit, is B= -3.12. However as discussed previously, B equals -6.8 x $10^{11}\Phi^{3/2}$/ β    (Φ in eV, ε  in V/μm and J in Amp/cm$^2$).

Setting these expressions to be equal and considering the appropriate conversions in units, we extract an amplification factor of β= 20 x $10^6$. The Si work function was set at 4.5 eV in all calculations made.

The macroscopic enhancement of the tips can be evaluated by dividing the tip height by the tip radius. Considering the spikes density for the specific experimental conditions applied we extract a total enhancement of about 4.4 x $10^6$. The difference in the total enhancement factor calculated through the slope of the linear Fowler-Nordheim plot and the evaluation of the macroscopic enhancement

of the tips may be attributed to the presence of narrow conducting channels in the SiO$_x$ matrix in the microtip body, as has been indicated by Shafeev et. al. [59,60]. Also in recent work by Crouch et. al. [61] The cross sections of structures obtained utilizing both ns and fs laser sources were examined by implementing the bright – field transmission electron microscopy (TEM). They have found that the cone surfaces are covered by a highly disordered layer of Si (including nanocrystallites, nanopores, and sulfur impurities) that is 1μm thick in the case of the fs laser source and less than 200nm in the case of the ns laser source. tips on the cone bodies.

In general it is expected that the details of the surface morphology will influence the electron field emission and to this effect the presence of secondary tips with dimensions of a few tens of nanometers, on the cone tip bodies, should also be taken into account. Based on these considerations, there is a good agreement between the experimental field emission and evaluated geometrical field enhancement.

Finally, the dependence of field emission on the uniformity of spikes (average height, average tip radius, density and distribution over the microstructured area e.t.c.), may influence the results obtained and should also be considered. Along these lines, in the more recent data, care has been taken for obtaining spikes of high uniformity by selecting optimal processing conditions (e.g. overlap between consecutive scans). However no further field emission measurements are available at this point.

# CHAPTER 6

## CONCLUDING REMARKS & FUTURE ASPECTS

### 6.1 CONCLUDING REMARKS

This thesis has exhibited the possibility of utilizing laser sources for the fabrication of high aspect ratio, quasi-periodical arrays of Si microtips in the presence of a reactive gas ($SF_6$). These structures exhibit exceptional field emission properties, which may be utilized as the basis for directional electron emitter devices, opening up in this way a number of technological applications of interest.

The main objective of this work has been the optimisation of the morphology and field emission properties of laser produced Si microstructures. Utilizing different laser and reactive gas parameters aspect ratio maximization in a controlled manner, on the basis of homogeneity, was aimed.

Three laser sources with different pulse duration (ns, sub-ps, fs) have been employed for the purposes of this work. The obtained samples were characterized morphologically by means of SEM (Scanning Electron Microscopy). Moreover field emission testing on the microstructured surfaces was performed.

The outcome of this work is summarized as follows:

- The aspect ratio, density and curvature of the obtained structures depends strongly on the laser parameters employed (e.g. laser wavelength, pulse duration).

- Similar trends in spikes growth are observed, independently of the laser source employed. More specifically, in all cases, a decrease in spikes density with increasing laser fluence and an increase in their height with increasing number of pulses, is observed

- The role of the reactive gas ($SF_6$) pressure appears to be crucial as far as the morphology and quality of the obtained Si microstructures is concerned. The spikes grown in vacuum were blunt in all cases, however they became better defined and more pronounced with increasing $SF_6$ pressure. The presence of secondary tip decoration with a diameter of a few tens of nanometers on the cone bodies, was evident with all the laser sources employed.

- The highest aspect ratio of the fabricated Si microcolumns was obtained using the Ti:Sapphire laser source. Under the best conditions, a tip diameter as low as **500nm** with a height up to **30µm** was observed.

- A field emission threshold as low as **2V/µm**, with an emission current of $10^{-3}$ A/cm$^2$ at 4 V/µm., was observed for structures obtained using the ultrafast Ti:Sapphire laser source.

This work among others, has underlined the potential of utilizing laser-based methods in the fabrication of microstructures, for electron emitting devices. This means of microstructuring may open up new possibilities, in terms of functionality, in the field of vacuum microelectronics.

## 6.2 FUTURE ASPECTS

The electrical properties of microstructured Si in the presence of a reactive gas (such as $SF_6$) as well as prospects of their exploitation have been discussed extensively. However the potential of exploiting their optical properties should be considered as well. Increased absorptance of light by Si to approximately 90% from the near ultraviolet (0.25 µm) to the near infrared (2.5 µm) by surface microstructuring utilizing laser pulses in the presence of SF6 and other reactive gases, has been observed by Carey et. al. [62]. It appears that production of sulfur impurities is responsible for the formation of a band of infrared-absorbing states. Additionally, due to the surface texture, multiple reflections of light in the cones occur. In this way, the reflectance is significantly reduced and consequently the absorption throughout the above mentioned wavelengths, is increased. These remarkable properties may be exploited for the fabrication of solar batteries, as

well as for Si-based detectors for infrared radiation. A new functionality for Si is acknowledged on this basis, as the exploitation of both optical and electric properties, could expand the use of inexpensive Si in new field areas, such as optoelectronics.

Additional interest lies in the formation of regular arrays of Si microspikes by laser irradiation through a mask [63]. These ordered arrays of microspikes obtained, could find application as pixels of microspikes for field emission devices and detectors.

Finally, recent interest has been placed on the fabrication of ordered arrays of silicon cones by optical diffraction techniques in the presence of $SF_6$ [64]. This work puts into evidence the prospective of spatially (in one dimension) controlling the location of the structures via near-field diffraction of the incident beam, in terms of periodicity and homogeneity over the laser microstructured area.

# REFERENCES

[1] H.H.Busta, *J.Micromech.Microeng*. **2**, 43 (1992)

[2] C.A.Spindt, *J.Appl.Phys* **39**, 1968, 3504

[3] R. Gomer, *Field Emission and Field Ionization* (Harvard University Press, Massachusetts, US, 1961)

[4] H.Z. Busta, *J. Microeng.* **2**, 43 (1992)

[5] D.W. Tuggle, J.Z. Li, L.W. Swanson, *J.Microscopy* **140**, 293

[6] C.Wang, A.Garcia, D.C.Ingram, M.Lake, M.E.Kordesch, *Electronic Letters* **27**, 1459 (1991)

[7] R.Waters, B.Van. Zeghbroeck, *Appl. Phys. Lett.* **75**, 2410 (1999)

[8] R. Forbes, *Solid State Elec.* **45**, 779 (2001)

[9] T.Utsumi, Keynote address-vacuum microelectronics: "What's new and exciting", *IEEE T-ED* **38**, 2276 (1991)

[10] D.Nicolaescu, Romanian Journal of Information Science and Technology **3**(2), 129 (2000)

[11] E.Jansen, R. Stedman, G.Grossman, H.G. Grimmeiss, *Phys. Rev. B* **29**, 1907 (1984)

[12] S.Nolte, C.Momma, H.Jacobs, A.Tunnermann, B.N. Chikov, B. Wellegehausen, H.Welling, *J.Opt.Soc. Am. B* **14**, 2716 (1997)

[13] A.K.Jain, V.N.Kulkarni, D.K.Sood, J.S.Uppol, *J.Appl.Phys* **52**, 4882 (1981)

[14] J.F.Young, J.S. Preston, H.M. van Driel, J.E. Sipe, *Phys. Rev. B* **27**, 1155 (1983)

[15] M. Henyk, N. Vogel, D. Wolfframmm, A. Tempel, J. Reif, *Appl. Phys. A* **69,** S-355 (1999)

[16] D.von der Linde, K.Sokolowski-Tinten, J. Bialkowski, *Appl. Surf. Sci.* **109/110**, 1 (1997)

[17] A.C. Tien, S. Backus, H. Kapteyn, M. Mourane, G. Mourou, *Phys. Rev. Lett.* **82**, 3883 (1999)

[18] P.C.Becker, H.L.Fragnito, C.H.Brito Cruz, R.L. Fork, J.E. Cunningham, J.E.Henry, C.V.Shank, *Phys. Rev. Lett.* **61**, 1647 (1988)

[19] K.L. Saenger, *Processing of Advanced Matreials* **3**, 63 (1993)

[20] J.F.Young, J.S. Preston, H.M. van Driel and J.E. Sipe, , *Phys. Rev. B* **27**(2) , 1155, 1983

[21] M. Birnbaum, *J. Appl. Phys.* **36**, 3688 (1965)

[22] H.J. Leamy, G.A. Rozgonyi, T.T. Sheng, G.K. Celler, *Appl. Phys. Lett.* **32**, 535 (1978)

[23] G.N. Maracas, G.L. Harris, C.A. Lee, R.A. McFarlane, *Appl. Phys. Lett.* **33**, 453 (1978)

[24] N.R. Isenor, *Appl. Phys. Lett.* **31**, 148 (1977)

[25] A. K. Jain, V.N. Kulkarni, D.K. Sood, J.S. Uppol, *J. Appl. Phys.* **52**, 4882 (1981)

[26] J. Reif, F. Costache, M. Henyk, S.V. Pandelov, *Appl. Surf. Sci.* **197**, 891 (2002)

[27] F. Costache, M. Henyk, J. Reif, *Appl. Surf. Sci.* **208**, 486 (2003)

[28] F. Keliman, *Phys. Rev. Lett.* **51**, 2079 (1983)

[29] D.Bauerle, *Laser Processing and Chemistry*, Third Edition, Springer-Verlag Berlin Heidelberg New York (2000)

[30] M. Birnbaum, *J.Appl. Phys.* **36**, 3688 (1965)

[31] S. Clark, D.C. Emmony, *Phys. Rev. B.* **40**, 2031 (1989)

[32]  J.F.Young, J.E. Sipe, H.M. van Driel, *Phys. Rev. B* **30**(4) , 2001, 1984

[33]  L.D. Landau and E.M.Lifshitz, *Fluid Mechanics* (Pergamon, London, 1959)

[34]  A.J. Pedraza, J.D. Fowlkes, S. Jesse, C. Mao, D.H. Lowndes, *Appl. Surf. Science* **168**, 251 (2000)

[35]  M.Y. Shen, C.H. Crouch, J.E. Carey, R. Younkin, E. Mazur, M. Sheehy, C.M. Friend, *Appl. Phys.Lett.* **82**(11), 1715 (2003)

[36]  E. Janniti, A.M. Malvezzi, G. Tondello, *J. Appl.Phys.* **46**, 3096 (1975)

[37]  S.I Dolgaev, S.V. Lavrishev, A.A. Lyalin, A.V. Simakin, V.V. Voronov, G.A. Shafeev, *Appl. Phys. A* **73**, 177 (2001)

[38]  J.E.Carey, C.H.Crouch, E.Mazur, *Optics and Photonics News,* 32, 2/2003

[39]  F.Sanchez, J.L.Morenza, R.Aguiar, J.C.Delgado, M.Varela, *Appl. Phys. Lett.* **69**(5) (1996) 620.

[40]  F.Sanchez, J.L.Morenza, R.Aguiar, J.C.Delgado, M.Varela, *Appl. Phys. A* **66** (1996) 83.

[41]  A.J.Pedraza, J.D.Fowlkes, D.H.Lowndes, *Appl. Phys. Lett.* **74**(16) (1999) 2322.

[42]  J.D.Fowlkes, A.J.Pedraza, D.H.Lowndes, *Appl. Phys. Lett.* **77**(11) (2000) 1629.

[43]  T-H.Her, R.J.Finlay, C.Wu, S.Deliwala, E.Mazur, *Appl. Phys. Lett.* **73**(12) (1998) 1673.

[44]  T-H.Her, R.J.Finlay, C.Wu, E.Mazur, *Appl. Phys. A* **70** (2000) 383.

[45]  A.V. Karabutov, V.D. Frolov, E.N. Loubnin, A.V. Simakin, G.A. Shafeev, *Appl. Phys. A* **76**, 413 (2003)

[46]  A.A. Evtukh, E.B. Kaganovich, V. G. Litovchenko, Yu.M. Litvin, D.V. Fedin, E.G. Manoilov, S.V. Svechnikov, Semiconductor Physics, *Quantum Electronics & Oproelectronics*, **3(4),** 474 (2000).

[47]  D.Riedel, J.L.Hernandez-Pozos, R.E.Palmer, K.W. Kolasinski, to be published at *Appl. Phys. A.*

[48]  S. Szatmári and F. P. Schäfer, *Optics Communications* **68**, 196 (1988).

[49]  P. Simon, H. Gerhardt, S. Szatmári, *Optics Communications* **71**, 305 (989).


[50]  D.H. Lowndes, J.D. Fowlkes, A.J. Pedraza, *Appl. Surf. Science* **154**, 647 (2000)

[51]  T-H. Her, R.J. Finlay, C. Wu, S. Deliwala, E. Mazur, *Appl. Phys. Lett.* **73(12)**, 1673 (1998)

[52]  M.Y Shen, C.H. Crouch, J.E. Carey, R. Younkin, E. Mazur, M. Sheehy, C.M. Friend, *Appl. Phys. Lett.* **82(11)**, 1715 (2003)

[53]  D.H.Lowndes, J.D.Fowlkes, A.J.Pedraza, *Appl. Surf. Sc*i. **154-155** 647 (2000)

[54]  F.Sanchez, J.L.Morenza, R.Aguiar, J.C.Delgado, M.Varela, *Appl. Phys. A* **66,** 83 (1996)

[55]  T-H.Her, R.J.Finlay, C.Wu, E.Mazur, *Appl. Phys. A* **70**, 383 (2000)

[56]  J.D.Fowlkes, A.J.Pedraza, D.H.Lowndes, *Appl. Phys. Lett.* **77(11),** 1629 (2000)

[57]  G. Herzberg, *"Molecular Spectra and Molecular Structure III"*. ("Electronic Spectra and Electronic Structure of Polyatomic Molecules") 1966 Van Nostrand Reinhold Company, New York

[58]  C.Wu, PhD thesis-Harvard (20001)

[59]  A.V. Karabutov, V.D. Frovol, A.V. Simakin, G.A. Shafeev, *J.Vac.Sci.Technol.B* **21(1)**, 449 (2003)

[60]  Karabutov AV, Frolov VD, Loubnin EN, Simakin AV, Shafeev GA *Appl.Phys.A* **76**, 413 (2003)

[61]  C.H. Crouch, J.E. Carey, J.M. Warrender, M.J. Aziz, E. Mazur, to appear in *Appl.Phys.Lett.*

[62]  J.E.Carey, C.H.Crouch, E.Mazur, *Optics and Photonics News*, 32, **2**/2003

[63]  M.Y Shen, C.H. Crouch, J.E. Carey, R. Younkin, E. Mazur, M. Sheehy, C.M. Friend, *Appl. Phys. Lett*. **82(11),** 1715 (2003)

[64]  D.Riedel, J.L.Hernandez-Pozos, R.E.Palmer, K.W. Kolasinski, to be published at *Appl. Phys. A.*